Space Sci Rev (2019) 215:50
https://doi.org/10.1007/s11214-019-0613-y

Lunar Seismology: An Update on Interior Structure Models

Raphael F. Garcia[1,2] · Amir Khan[3] · Mélanie Drilleau[4] · Ludovic Margerin[2] · Taichi Kawamura[4] · Daoyuan Sun[5,6] · Mark A. Wieczorek[7] · Attilio Rivoldini[8] · Ceri Nunn[9,10] · Renee C. Weber[11] · Angela G. Marusiak[12] · Philippe Lognonné[4] · Yosio Nakamura[13] · Peimin Zhu[14]

Received: 7 March 2019 / Accepted: 4 October 2019

Abstract An international team of researchers gathered, with the support of the International Space Science Institute (ISSI), (1) to review seismological investigations of the lunar interior from the Apollo-era and up until the present and (2) to re-assess our level of knowledge and uncertainty on the interior structure of the Moon. A companion paper (Nunn et al. in Space Sci. Rev., submitted) reviews and discusses the Apollo lunar seismic data with the aim of creating a new reference seismic data set for future use by the community. In this study, we first review information pertinent to the interior of the Moon that has become

Electronic supplementary material The online version of this article (https://doi.org/10.1007/s11214-019-0613-y) contains supplementary material, which is available to authorized users.

✉ R.F. Garcia
raphael.garcia@isae.fr

1 Institut Supérieur de l'Aéronautique et de l'Espace (ISAE-SUPAERO), Université de Toulouse, 10 Ave E. Belin 31400 Toulouse, France

2 Institut de Recherche en Astrophysique et Planétologie, C.N.R.S., Université de Toulouse, 14 Ave E. Belin, 31400 Toulouse, France

3 Institute of Geophysics, ETH Zürich, Zürich, Switzerland

4 Institut de Physique du Globe de Paris,UniversitÃl' de Paris, CNRS, 75005 Paris, France

5 Laboratory of Seismology and Physics of EarthâĂŹs Interior, School of Earth and Space Sciences, University of Science and Technology of China, Hefei, China

6 CAS Center for Excellence in Comparative Planetology, Hefei, China

7 Laboratoire Lagrange, Observatoire de la Côte d'Azur, CNRS, Université Côte d'Azur, Nice, France

8 Observatoire Royal de Belgique, 3 Avenue Circulaire, 1050 Bruxelles, Belgium

9 Jet Propulsion Laboratory, California Institute of Technology, Pasadena, USA

10 Ludwig Maximilian University, Munich, Germany

11 NASA Marshall Space Flight Center, Huntsville, AL, USA

12 University of Maryland, College Park, MD, USA

Published online: 07 November 2019

available since the Apollo lunar landings, particularly in the past ten years, from orbiting spacecraft, continuing measurements, modeling studies, and laboratory experiments. Following this, we discuss and compare a set of recent published models of the lunar interior, including a detailed review of attenuation and scattering properties of the Moon. Common features and discrepancies between models and moonquake locations provide a first estimate of the error bars on the various seismic parameters. Eventually, to assess the influence of model parameterisation and error propagation on inverted seismic velocity models, an inversion test is presented where three different parameterisations are considered. For this purpose, we employ the travel time data set gathered in our companion paper (Nunn et al. in Space Sci. Rev., submitted). The error bars of the inverted seismic velocity models demonstrate that the Apollo lunar seismic data mainly constrain the upper- and mid-mantle structure to a depth of ∼1200 km. While variable, there is some indication for an upper mantle low-velocity zone (depth range 100–250 km), which is compatible with a temperature gradient around 1.7 °C/km. This upper mantle thermal gradient could be related to the presence of the thermally anomalous region known as the Procellarum Kreep Terrane, which contains a large amount of heat producing elements.

Keywords Moon · Seismology · Internal structure of planets

1 Introduction

Geophysical investigation of the Moon began with the manned Apollo lunar missions that deployed a host of instruments including seismometers, surface magnetometers, heat-flow probes, retroreflectors, and a gravimeter on its surface. Much of what we know today about the Moon comes from analysis of these data sets that have and are continuously being complemented by new missions since the Apollo era.

Of all of the geophysical methods, seismology provides the most detailed information because of its higher resolving power. Seismometers were deployed on the lunar surface during each of the Apollo missions. Four of the seismic stations (12, 14, 15, and 16), which were placed approximately in an equilateral triangle (with corner distances of ∼1100 km), operated simultaneously from December 1972 to September 1977. During this period, more than twelve thousand events were recorded and catalogued with the long-period sensors including shallow and deep moonquakes and meteoroid and artificial impacts (e.g., Toksoz et al. 1974; Dainty et al. 1974; Lammlein 1977; Nakamura 1983). In addition, many more thermal quakes were also recorded with the short-period sensors (Duennebier and Sutton 1974). That the Moon turned out to be so "active" came as somewhat of a surprise. A common notion prior to the lunar landings was partly reflected in Harold Urey's belief that the Moon was a geologically dead body (Urey 1952). At the time, only meteoroid impacts were expected to be recorded from which the internal structure of the Moon would be deduced. The existence of deep and shallow moonquakes was a serendipitous discovery—not accidental, but fortuitous and did much to improve models of lunar internal structure (see e.g., Nakamura 2015, for a historical account).

[13] Institute for Geophysics, John A. and Katherine G. Jackson School of Geosciences, University of Texas at Austin, Austin, TX, USA

[14] China University of Geosciences, Wuhan, China

The moonquakes are typically very small-magnitude events. The largest shallow moonquake has a body-wave magnitude of about 5, whereas the deep moonquakes have magnitudes less than 3 (Goins et al. 1981). That so many small-magnitude events could be observed at all is a combined result of the performance of the seismic sensors and the quiescence of the lunar environment, as neither an ocean nor an atmosphere is present to produce micro-seismic background noise.

The lunar seismic signals were found to be of long duration and high frequency content. These characteristics of lunar seismograms are related to intense scattering in a highly heterogeneous, dry, and porous lunar regolith and to low instrinsic attenuation of the lunar interior (this will be discussed in more detail in the following). This complexity, in combination with the scarcity of usable seismic events and small number of stations inevitably led to limitations on the information that could be obtained from the Apollo lunar seismic data (Toksoz et al. 1974; Goins 1978; Nakamura 1983; Khan and Mosegaard 2002; Lognonné et al. 2003; Garcia et al. 2011). In spite of the "difficulties" that beset this data set, it nonetheless constitutes a unique resource from which several models of the lunar velocity structure have been and continue to be obtained. For this reason, it is considered important to gather the various processed data sets and published models and to synthesize our current knowledge of lunar internal structure in order to provide a broad access to this data set and models.

In addition to the seismic data, models of the lunar interior are also constrained by other geophysical data acquired during and after the Apollo missions—an endeavour that continues to this day either in-situ (through reflection of laser light on corner cube reflectors) or through orbiting satellite missions. These data, which are also considered in the following, include gravity and topography data, mass, moment of inertia, Love numbers (gravitational and shape response), electromagnetic sounding data and high pressure experiments that individually or in combination provide additional information on the deep lunar interior (Williams et al. 2001a, 2014; Zhong et al. 2012; Wieczorek et al. 2013; Shimizu et al. 2013; Besserer et al. 2014).

The authors of this paper are members of an international team that gathered in Bern and Beijing and were sponsored by the International Space Science Institute. The team convened for the purpose of gathering reference data sets and a set of reference lunar internal structural models of seismic wave speeds, density, attenuation and scattering properties. This work is summarized in two papers: this paper reviews and investigates lunar structural models based on geophysical data (seismic, geodetic, electromagnetic, dissipation-related) and the companion paper (Nunn et al. submitted) reviews the Apollo lunar seismic data. More specifically, in this study we compile and re-assess recent improvements in our knowledge of the lunar interior, including lunar geophysical data, models, and miscellaneous information that bears on this problem. All of these models embrace diverse parameterisations and data that are optimized for the purpose of addressing a specific issue. The question therefore arises as to the accuracy and consistency of the results if the different parameterisations are viewed from the point of view of a single unique data set. To address this issue, we re-investigate the problem of determining interior structure from the newly derived Apollo lunar seismic data described in our companion study (Nunn et al. submitted) using a suite of different model parameterisations. For complimentary aspects of lunar geophysics, seismology, and interior structure, the reader is referred to reviews by Lognonné and Johnson (2007) and Khan et al. (2013).

2 Constraints on the Lunar Interior from Geophysical Observations, Modeling Studies, and Laboratory Measurements

2.1 Shape, Mass, Moment of Inertia, and Love Numbers

Radio tracking of lunar orbiting spacecraft, altimetry measurements from orbit, and analysis of Lunar Laser Ranging (LLR) data constrain a variety of global quantities that bear on the Moon's interior structure. These parameters include the average radius of the surface, the total mass, the moments of inertia of the solid portion of the Moon, and Love numbers that quantify tidal deformation.

The product of the lunar mass and gravitational constant GM is best determined by the Jet Propulsion Laboratory DE403 ephemeris (Williams et al. 2013) that is based on a combination of spacecraft and LLR data. This solution yields a value of the lunar mass of $M = (7.34630 \pm 0.00088) \times 10^{22}$ kg, where the uncertainty is dominated by the uncertainty in the gravitational constant (Williams et al. 2014). The shape of the Moon has been mapped by orbiting laser altimeters, of which the most successful was the instrument LOLA (Lunar Orbiter Laser Altimeter, Smith et al. 2010) that was flown on the Lunar Reconnaissance Orbiter (LRO) mission. The average radius R of the Moon from the LOLA data is 1737.151 km (Wieczorek 2015), which is uncertain by less than 1 m. Combining these two quantities provides the average density of the Moon, which is $\bar{\rho} = 3345.56 \pm 0.40\ \mathrm{kg\,m^{-3}}$.

The response of the Moon to tides is quantified by Love numbers that depend upon the spherical harmonic degree and order of the tidal potential. The ratio of the induced potential to the tidal potential is given by the Love number k, whereas the ratio of the surface deformation to the tidal potential is proportional to the Love number h. For spherical harmonic degree 2, there are 5 independent Love numbers, and GRAIL analyses have solved for three of them: k_{20}, k_{21} and k_{22} (Konopliv et al. 2013; Lemoine et al. 2013) (the sine and cosine terms of the latter two were assumed to be equal). The three degree-2 Love numbers are approximately equal, and the uncertainty is reduced when solving only for a single value that is independent of angular order. Two independent analyses of the GRAIL data provide concordant values of $k_2 = 0.02405 \pm 0.00018$ (Konopliv et al. 2013) and $k_2 = 0.024116 \pm 0.000108$ (Lemoine et al. 2014). Following Williams et al. (2014), we make use of an unweighted average of the two values and uncertainties, which yields $k_2 = 0.02408 \pm 0.00014$. Analyses of the GRAIL data also provide estimates of the degree-3 Love numbers, though with larger uncertainties: $k_3 = 0.0089 \pm 0.0021$ (Konopliv et al. 2013) and $k_3 = 0.00734 \pm 0.0015$ (Lemoine et al. 2013). It should be noted that the k_2 and k_3 Love numbers were calculated using a reference radius of $R_0 = 1738$ km. To obtain the corresponding values using the average radius of the Moon, it is necessary to multiply the k_2 values by $(R_0/R)^5$ and the k_3 values by $(R_0/R)^7$.

The moments of inertia of the Moon are uniquely determined by the large scale distribution of mass below the surface. Differences of the three principal moments are given by the degree-2 spherical harmonic coefficients of the gravitational potential. Ratios of the moments play an important role in quantifying time-variable physical libration signals that arise from tidal torques, and these can be determined from analyses of LLR data. The rotation of the Moon depends on the k_2 and h_2 Love numbers, the low degree spherical harmonic coefficients of the gravity field, and sources of energy dissipation. Two sources of energy dissipation have been found necessary to account for the LLR data: solid body dissipation as quantified by a frequency dependent quality factor Q, and viscous dissipation at the interface between a fluid core and solid mantle (see Williams et al. 2014; Williams and Boggs 2015).

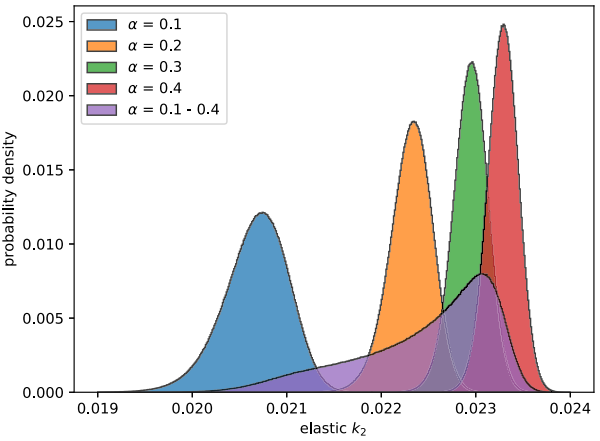

Fig. 1 Probability distributions of the elastic k_2 Love number for different values of α. Q is assumed to have a power law dependence on frequency with exponent α, and the distributions are plotted using constant values of 0.1, 0.2, 0.3, and 0.4. Also plotted is a case where all values of α 0.1 to 0.4 are equally probable

In the analyses of the LLR data, the absolute values of the moments of inertia of the fluid core are not well constrained. Nevertheless, differences between the core principal moments are detected, as is the viscous coupling constant. The moments of inertia of the solid portion of the Moon are tightly constrained, with an average value of $I_s/MR_0^2 = 0.392728 \pm 0.000012$ (Williams et al. 2014). Here, the average moment was normalized using a radius of $R_0 = 1738$ km, and to normalize the moments to the physical radius of the Moon, it is only necessary to multiply this value by $(R_0/R)^2$, which gives $I_s/MR^2 = 0.393112 \pm 0.000012$. Williams and Boggs (2015) constrain the quality factor to be $Q = 38 \pm 4$ at monthly periods and 41 ± 9 at yearly periods. The Q appears to increase for longer periods, but only lower bounds of 74 and 56 are obtained for periods of 3 and 6 years, respectively. Lastly, the LLR analyses constrain the monthly degree-2 Love number to be $h_2 = 0.0473 \pm 0.0061$. Independent analyses of orbital laser altimetry have been used to investigate the tidal response of the Moon. LOLA altimetric crossovers show a monthly signal that arises from tides, and this signal constrains the h_2 Love number to be 0.0371 ± 0.0033 (Mazarico et al. 2014), which is somewhat smaller than the value obtained from analyses of the LLR data.

The k_2 and h_2 Love numbers are in general frequency dependent. The orbital measurements are most sensitive to monthly periods and it has been recognized that there are non-negligeable anelastic contributions to the Love numbers at these frequencies (e.g., Nimmo et al. 2012; Khan et al. 2014). When inverting for interior structure, it is convenient to estimate the purely elastic component in the infinite-frequency limit by removing the anelastic contribution. One technique that has been used to do so is to assume that the dissipation is both weak and frequency dependent with $Q \sim \omega^{\alpha}$, where ω is frequency and α is somewhere between 0.1 and 0.4 (e.g., Khan et al. 2014; Matsuyama et al. 2016).

Using the measured monthly values of k_2 and Q, the probability distribution of the predicted k_2 elastic Love number is plotted in Fig. 1 for four different values of α. The average value of the elastic k_2 is seen to increase from 0.206 to 0.232 as α increases from 0.1 to 0.4. Furthermore, the rate of change of the distributions decreases as α increases. If it is assumed that all values of α from 0.1 to 0.4 are equally probable (as in Matsuyama et al. 2016), the distribution is found to be highly non-Gaussian, with a mode at 0.02307 and a 1σ confidence interval of $[0.02169, 0.02316]$. Using a value of $\alpha = 0.3$ (as in Khan et al. 2014), we find a value of 0.02294 ± 0.00018. Anelastic corrections for the k_2 and h_2 Love number are presented in Table 5 using a value of $\alpha = 0.3$.

2.2 Crustal Thickness, Density, and Porosity

Analyses of high resolution gravity data from the GRAIL spacecraft have been able to constrain the density and porosity of the lunar crust. The analysis procedure makes use of the fact that short wavelength density variations in the crust generate gravity anomalies that rapidly attenuate with increasing depth below the surface, and that the gravitational signal of lithospheric flexure is unimportant for the shortest wavelengths. In the analysis of Wieczorek et al. (2013), it was assumed that the density of the crust was constant, and the bulk density was determined by the amplitude of the short wavelength gravity field. This approach provided an average bulk crustal density of 2550 kg m^{-3}, and when combined with estimates for the density of the minerals that compose the crust, this implies an average porosity of about 12%.

As a result of the assumptions employed in the above analysis, the bulk crustal density and porosity determinations should be considered to represent an average over at least the upper few km of the crust. An alternative analysis that attempted to constrain the depth dependence of density (Besserer et al. 2014) implies that significant porosity exists several 10s of km beneath the surface. The closure of pore space at depth was argued to occur primarily by viscous deformation (Wieczorek et al. 2013), which is a temperature dependent process. Using representative temperature gradients over the past 4 billion years, porosity is predicted to decrease rapidly over a narrow depth interval that lies somewhere between about 45 and 80 km depth. Thus, significant porosity could exist not only in the crust, but also in the uppermost mantle.

Lastly, we note that it is possible to invert for both the average thickness of the crust and lateral variations in crustal thickness using gravity and topography data (e.g., Wieczorek 2015). These models, however, require knowledge of not only the density of the crust and mantle, but also an independent constraint on the crustal thickness at one or more locations. In the GRAIL-derived crustal thickness model of Wieczorek et al. (2013), the crustal thickness was constrained to be either 30 or 38 km in the vicinity of the Apollo 12 and 14 landing sites based on the seismic determinations of Lognonné et al. (2003) and Khan and Mosegaard (2002), respectively. The density of the mantle of this model was varied in order to achieve a crustal thickness close to zero in the center of the Crisium and Moscoviense impact basins, which are both thought to have excavated through the crust and into the mantle (see Miljković et al. 2015). In these models, the average crustal thickness was found to be either 34 or 43 km, based on the thin and thick seismic determinations, respectively. In addition, the density of the uppermost mantle was constrained to lie between 3150 and 3360 kg m^{-3}, allowing for the possibility of a maximum of 6% porosity in the uppermost mantle.

2.3 Mantle Temperature and Electrical Conductivity Structure

Electromagnetic sounding data have been inverted to constrain the conductivity profile of the lunar interior (Sonett 1982; Dyal et al. 1976; Hood et al. 1982; Hobbs et al. 1983), and have also been used to put limits on the present-day lunar temperature profile (Duba et al. 1976; Huebner et al. 1979; Hood et al. 1982; Khan et al. 2006b; Karato 2013). Electromagnetic sounding data in the form of lunar day-side transfer functions (Hobbs et al. 1983) measure the lunar inductive response to external magnetic fields that change in time during intervals when the Moon is in the solar wind or terrestrial magnetosheath (Sonett 1982). The transfer function data (Table 6) depend on frequency such that long-period signals are sensitive to deeper structure, while shorter periods sense the shallow structure. Limits on the

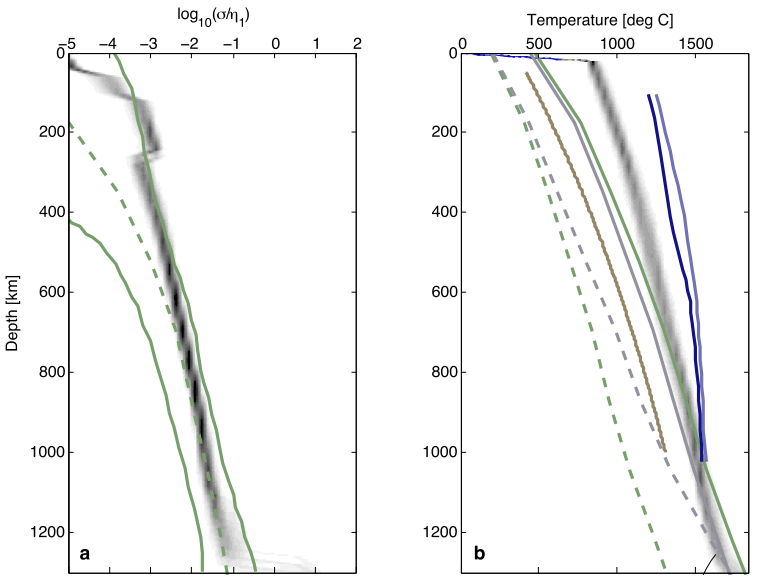

Fig. 2 Lunar mantle electrical conductivity (a) and thermal (b) profiles. In (**a**) green lines show the mean Apollo-era conductivity model and range of conductivities determined by Hood et al. (1982), whereas the contoured probability distributions are from Khan et al. (2014). In (**b**) the thermal profiles from Karato (2013) are based on dry olivine (solid gray line), dry orthopyroxene (solid green line), hydrous olivine (0.01 wt % H_2O, dashed gray line), and hydrous orthopyroxene (0.01 wt % H_2O, dashed green line). Contoured probability distributions are from Khan et al. (2014). Also included here is the lunar mantle geotherm of Kuskov and Kronrod (2009) and the solidii of Longhi (2006) for two lunar compositions: lunar primitive upper mantle (dark blue) and Taylor Whole Moon (light blue), respectively. $\eta_1 = 1$ S/m. Modified from Khan et al. (2014)

lunar geotherm can be derived from the inferred bounds on the lunar electrical conductivity profile based on the observation that laboratory mineral conductivity measurements depend inversely on temperature.

Figure 2a compiles the electrical conductivity models of Khan et al. (2014), Hood et al. (1982) and Karato (2013). The former is obtained from inversion of the lunar induction data described above and global geodectic data (M, I/MR^2, and k_2) in combination with phase equilibrium modeling (see Sect. 6.1 for more details), while the model of Hood et al. (1982) derives inversion of induction data only, whereas Karato (2013) combines Apollo-era electrical conductivity models with constraints from tidal dissipation (Q). When combined with mantle mineral electrical conductivity measurements, the phase equilibrium models (including density, seismic wave speed, and temperature profiles) can be turned into laboratory-based electrical conductivity models that can be tested against the available data. In contrast, Karato (2013) considers the mean Apollo-era conductivity profile derived by Hood et al. (1982) (dashed line in Fig. 2a) and tidal dissipation (Q) to constrain water and temperature distribution in the lunar mantle. Models are constructed on the basis of laboratory data and supplemented with theoretical models of the effect of water on conductivity and dissipative (anelastic) properties of the mantle. The conductivity models of Karato (2013) are generally consistent with an anhydrous mantle, although small amounts of water cannot be ruled out.

Current constraints on lunar mantle temperatures are shown in Fig. 2b in the form of a suite of present-day lunar thermal profiles. These derive from the geophysical studies

of Khan et al. (2014), Karato (2013), and Kuskov and Kronrod (2009). The latter study combines the seismic model of Nakamura (1983) with phase equilibrium computations to convert the former to temperature given various lunar bulk compositions. These studies indicate that present-day mantle temperatures are well below the mantle solidii of Longhi (2006) (also shown in Fig. 2b) for depths $\leq$1000 km with average mantle thermal gradients of 0.5–0.6 °C/km, corresponding to temperatures in the range ~1000–1500 °C at 1000 km depth. Larger thermal gradients of about 1 °C/km were obtained in the same depth range by Gagnepain-Beyneix et al. (2006). For depths >1100 km, the mantle geotherms of Khan et al. (2014) and Karato (2013) (anhydrous case) cross the solidii indicating the potential onset of melting in the deep lunar mantle and a possible explanation for the observed tidal dissipation within the deep lunar interior observed by LLR (Williams et al. 2001b, 2014) (but see also Karato 2013 and Nimmo et al. 2012 for alternative views).

Principal differences between the various models relate to differences in (1) electrical conductivity database, including anhydrous versus hydrous conditions, and (2) conductivity structure. Differences in laboratory electrical conductivity measurements are discussed elsewhere (Karato 2011; Yoshino 2010; Yoshino and Katsura 2012), but the conductivity measurements of Karato are in general more conductive than those of Yoshino and Katsura (Khan and Shankland 2012). Because of the trade-off between water content and temperature on conductivity, the hydrous cases considered by Karato (2013) result in lower mantle temperatures. However, whether the lunar mantle is really hydrous remains an open question (Hauri et al. 2015). Lastly, Karato (2013) employs the Apollo-era conductivity model of Hood et al. (1982), which, overall, is less conductive in the upper 800 km of the lunar mantle than the model of Khan et al. (2014). There is also evidence for a partially molten lower mantle from geodetic and electromagnetic sounding data (Khan et al. 2014), and to some extent the Apollo seismic data (Nakamura et al. 1973; Nakamura 2005; Weber et al. 2011).

2.4 Core

A partial liquid state of the lunar core or lower mantle is required to explain the lunar laser ranging (LLR) measurements of the Moon's pole of rotation (e.g. Williams et al. 2001b). Analysis of the seismic data have hinted at the presence of a solid inner core (Weber et al. 2011), which, based on thermal evolution modeling, appears necessary to explain the occurrence of the early lunar dynamo (e.g., Laneuville et al. 2014, 2018; Scheinberg et al. 2015). The conditions for either a liquid core or a solid-inner liquid-outer core to exist, however, depend critically on the thermo-chemical conditions of the core. Table 1 compiles estimates of lunar core size and density that derive from geophysical data and modeling.

In order to allow for a present day liquid part in the core and to explain its average density (Table 1) light elements are required. The identity of those elements is still debated, but the most plausible candidates are carbon and sulfur. Evidence for sulfur or carbon is deduced from lunar surface samples, assumptions about the formation of the lunar core, and laboratory data about the partitioning of siderophile elements between silicate melts and liquid metal (e.g., Righter and Drake 1996; Rai and van Westrenen 2014; Chi et al. 2014; Steenstra et al. 2017; Righter et al. 2017). The presence of other light elements like silicon or oxygen in appreciable amounts is unlikely because of unfavorable redox conditions during core formation (e.g., Ricolleau et al. 2011). Both carbon and sulfur depress the melting temperature of iron significantly, allowing for a present-day liquid core (Fig. 3).

The density of liquid Fe–S and Fe–C as a function of light element concentration at lunar core pressures is shown in Fig. 3b. The density of liquid Fe–S has been calculated following

Table 1 Summary of lunar core size estimates, methods and data that have been used to constrain these. Abbreviations are as follows: $\rho_a(\omega)$ = frequency-dependent electromagnetic sounding data; M = mean mass; I/MR^2 = mean moment of inertia; k_2, h_2 = 2nd degree Love numbers; Q = global tidal dissipation; T_P, T_S = lunar seismic travel times; LLR = lunar laser ranging. Note that although a number of studies are indicated as using the same data, there can nonetheless be modeling and processing differences between the various studies

Core radius (km)	Core density (g/cm^3)	Data and/or method	Source
170–360	–	Apollo T_P, T_S	Nakamura et al. (1974)
250–430	–	Lunar prospector $\rho_a(\omega)$	Hood et al. (1999)
350–370	5.3–7	LLR data	Williams et al. (2001a)
350–400	6–7	M, I/MR^2, k_2, Q	Khan et al. (2004)
300–400	5–7	M, I/MR^2, k_2, h_2, Q	Khan and Mosegaard (2005)
340–350	5.7	M, I/MR^2, Apollo T_P, T_S	Khan et al. (2006a)
310–350	–	Apollo lunar seismograms	Weber et al. (2011)
340–420	4.2–6.2	Apollo T_P, T_S and seismograms, M, I/MR^2, k_2	Garcia et al. (2011)
310–370	5.7	Seismic model and M, I/MR^2	Kronrod and Kuskov (2011)
290–400	–	Kaguya and Lunar Prospector $\rho_a(\omega)$	Shimizu et al. (2013)
200–380	–	GRAIL gravity data and LLR	Williams et al. (2014)
330–380	4.5–5	Apollo $\rho_a(\omega)$, M, I/MR^2, k_2	Khan et al. (2014)
330–400	3.9–5.5	M, I/MR^2, k_2, Q, Apollo T_P, T_S	Matsumoto et al. (2015)
<330	6–7.5	Molecular dynamics simulations of Fe–S (3–10 wt% S) alloys	Kuskov and Belashchenko (2016)
310–380	5.2–6.7	Elastic data of liquid Fe–S alloys (10–27 wt% S)	Morard et al. (2018)

Morard et al. (2018). For liquid Fe–C an ideal solution model has been assumed with liquid Fe (Komabayashi 2014) and liquid Fe3.5wt%C (Shimoyama et al. 2016) as end-members. Compared to Fe–S, the density of Fe–C decreases significantly slower with increasing light element concentration and the amount of C that can be dissolved in liquid Fe is below about 7 wt% at the pressure–temperature conditions of the lunar core, whereas sulfur saturation in Fe occurs at significantly larger concentrations. Consequently, if carbon were the major light element, then the average core density cannot be significantly lower than 7000 kg/m^3. Moreover, a solid graphite layer could be present (Fei and Brosh 2014) in the upper part of the core below the core-mantle-boundary, since temperature was higher when the core formed and therefore the C saturation concentration somewhat larger.

If instead the principal light element were sulfur, the average density of the core of the Moon (Table 1) implies that its concentration could be above 27 wt%. Such large amounts, however, appear to be at odds with lunar dynamo models that rely on the formation of an inner core that crystallises from the bottom-up to explain the timing of the past dynamo (e.g. Laneuville et al. 2014; Scheinberg et al. 2015). Depending on the precise amount of sulfur, different scenarios are possible for the core of the Moon. If, for example, the sulfur concentration is below the eutectic, i.e., <25 wt% (Fig. 3), then the core is likely be completely molten today, although a small inner core forming through precipitation of iron snow in the

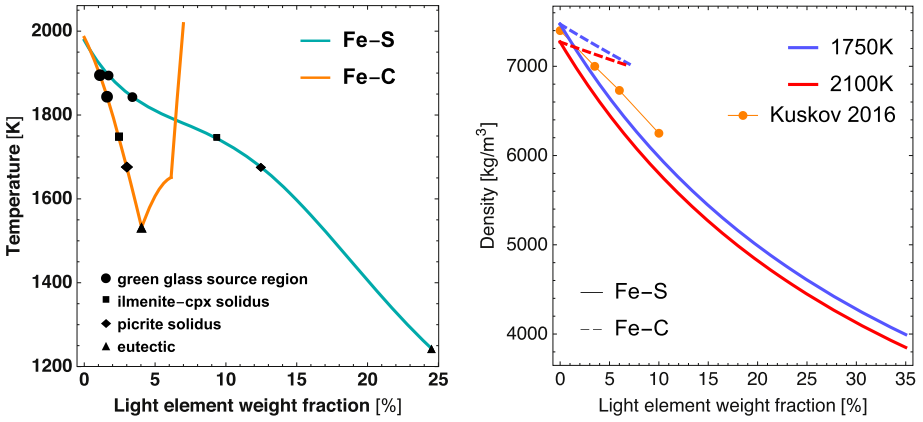

Fig. 3 Dependence of liquidi and density of Fe–S and Fe–C on light element content. (**a**) Iron-rich liquidus of Fe–S (Buono and Walker 2011) and liquidus of Fe–C (Fei and Brosh 2014) at 5 GPa. Symbols show candidate mantle solidi: green glass source (Longhi 2006), ilmenite-cpx (Wyatt 1977), picrite (Green et al. 1971), and the eutectic of Fe–S and Fe–C. (**b**) Density of liquid Fe–S and Fe–C at 5 GPa at two representative mantle temperatures (cf. Fig. 2b). The weight fraction of S is below the eutectic composition (∼25 wt%) and that of C is below its saturation (∼7 wt%). Orange circles are densities for Fe–S based on the molecular dynamics simulations of Kuskov and Belashchenko (2016) (at 5 GPa and 2000 K)

liquid part cannot be excluded. If, however, the S concentration is above the eutectic, then solid FeS will possibly crystallize and float to the top of the core.

Sulfur, however, appears to be disfavored by the most recent results based on thermochemical modeling (<0.5 wt% S) (Steenstra et al. 2017, 2018). Moreover, such sulfur-poor liquids, which correspond to densities around 7000 kg/m^3, imply present-day core temperatures around 2000 K and, as a consequence, significantly higher and, very likely too high, temperatures earlier on (e.g., Laneuville et al. 2014; Scheinberg et al. 2015). Depending on the lower mantle solidus, the requirement for either a molten or solid lower mantle, and the timing of the early lunar dynamo, the temperature at the core-mantle boundary has been estimated in the range ∼1500–1900 K. The lowest temperature in this range is below the Fe–C eutectic temperature at 5 GPa and would therefore imply a solid core if it were made of iron and carbon only. In comparison, present-day limits on the temperature of the deep lunar interior (∼1100 km depth) suggest temperatures in excess of 1800 K (Fig. 2b).

3 A Short Review of Published Seismic Velocity and Density Models

This section details some of the previously published models (those that are present in digital format). The specific data sets and prior information used to construct these models are summarized in Table 2. The amount of data used in the model inversions has noticeably increased with time. The tendency to include more global geophysical information (e.g., mass, moment of inertia, love numbers, electromagnetic sounding data) reflects the limitations inherent in the inversion of direct P- and S-wave arrival times in order to resolve lunar structure below ∼1200 km depth.

The seismic data collected during the 8 years that the lunar seismic stations were active have resulted in more than 12000 recorded events (Nunn et al. submitted) of which only

Table 2 Summary of data sets and prior information of previously published lunar models. Models are named as follows: TK74 == Toksoz et al. (1974), NK83 == Nakamura (1983), KM02 == Khan and Mosegaard (2002), LG03 == Lognonné et al. (2003), BN06 == Gagnepain-Beyneix et al. (2006), WB11 == Weber et al. (2011), GR11 == Garcia et al. (2011), KH14 == Khan et al. (2014) and MS15 == Matsumoto et al. (2015) NU19 == Nunn et al. (submitted). References cited in the Table are the following: KV73ab == Kovach and Watkins (1973a,b), H83 == Hobbs et al. (1983), VK01 == Vinnik et al. (2001)

Model	TK74	NK83	KM02	LG03	BN06	WB11	GR11	KH14	MS15	Best estimate
Data / prior										
Body wave travel times	P only KV73ab	P+S multiple	P+S NK83	P+S+Smp own+VK01	P+S+Smp LG03+VK01	S only own	P+S LG03	None	P+S LG03	ISSI team NU19
EM sounding	None	None	None	None	None	None	None	H83	None	H83
Prior source locations	KV73ab	None	None	None	None	LG03	LG03	None	LG03	ISSI team this paper
Mass ($\times 10^{22}$ kg)	None	None	None	None	None	None	7.3458	7.3463 $\pm$ 0.00088	7.34630 $\pm$ 0.00088	7.34630 $\pm$ 0.00088
I/MR^2	None	None	None	None	None	None	0.3932 $\pm$ 0.0002	0.393112 $\pm$ 0.000012	0.393112 $\pm$ 0.000012	0.393112 $\pm$ 0.000012
k_2	None	None	None	None	None	None	0.0213 $\pm$ 0.0025	0.0232 $\pm$ 0.00022	0.02422 $\pm$ 0.00022	0.02277 $\pm$ 0.00058 (elastic)
h_2	None	None	None	None	None	None	0.039 $\pm$ 0.008	None	None	0.048 $\pm$ 0.006
Prior crust seismic model	None	None	None	None	None	LG03	LG03	None	None	
Prior crust density	None	None	None	None	None	None	2.6–3.0	None	None	2.5–2.6

a subset were used to infer the lunar velocity structure (summarized in Table 2). Based on the final Apollo-era analyses of the two event data sets then available (Goins et al. 1981; Nakamura 1983), the major features of the lunar interior could be inferred to a depth of ∼1100 km. More recent reanalysis of the Apollo lunar seismic data using modern analysis techniques (Khan and Mosegaard 2002; Lognonné et al. 2003; Gagnepain-Beyneix et al. 2006) have largely confirmed earlier findings, but also added new insights (see below), while Nakamura (2005) expanded his original data set with an enlarged deep moonquake catalog.

In addition to the data obtained from the passive seismic experiment, active seismic experiments were also carried out during Apollo missions 14, 16, and 17 with the purpose of imaging the crust beneath the various landing sites (Kovach and Watkins 1973a,b; Cooper et al. 1974). The Apollo 17 mission carried a gravimeter that, because of instrumental difficulties, came to function as a short-period seismometer (Kawamura et al. 2015). Other seismological techniques to infer near-surface, crust, and deeper structure include analysis of receiver functions (Vinnik et al. 2001), noise cross-correlation (Larose et al. 2005; Sens-Schönfelder and Larose 2008), seismic coda (Blanchette-Guertin et al. 2012; Gillet et al. 2017), array-based waveform stacking methods (Weber et al. 2011; Garcia et al. 2011), and waveform analysis techniques based on spatial seismic wavefield gradients (Sollberger et al. 2016).

The one-dimensional seismic velocity and density models are compared in Fig. 4 and are provided as supplementary information in "named discontinuities" (nd) format. The recent velocity models of Khan and Mosegaard (2002), Lognonné et al. (2003), Gagnepain-Beyneix et al. (2006) are based on modern-day inversion (Monte Carlo and random search) and analysis techniques. The models of Khan and Mosegaard (2002), while relying on a Monte Carlo-based sampling algorithm (Markov chain Monte Carlo method) to invert the same data set considered by Nakamura (1983), provided more accurate error and resolution analysis than possible with the linearized methods available during the Apollo era. Lognonné et al. (2003) and Gagnepain-Beyneix et al. (2006) first performed a complete reanalysis of the entire data set to obtain independently-read arrival times and subsequently inverted these using random search of the model space. In all of the above studies both source location and internal structure were inverted for simultaneously.

Interpretation of Apollo-era seismic velocity models resulted in crustal thicknesses of 60 ± 5 km (Toksoz et al. 1974), but have decreased to 45 ± 5 km (Khan et al. 2000), 38 ± 3 km (Khan and Mosegaard 2002), and 30 ± 2.5 km (Lognonné et al. 2003).

Differences in crustal thickness estimates between Apollo-era and recent models are discussed in detail in Khan et al. (2013). They relate to the use of additional, but highly uncertain, body wave data (amplitudes, secondary arrivals, synthetic seismograms) in the seventies. Differences in crustal thickness between the recent models of Khan et al. (2000), Khan and Mosegaard (2002), and Lognonné et al. (2003) result from a combination of differences in travel time readings (data), inversion technique (methodology), and model parameterisation. Vinnik et al. (2001) also presented evidence for a shallower lunar crust-mantle boundary (28 km) through detection of converted phases below Apollo station 12.

Moving below the crust, mantle seismic velocity models are generally consistent to a depth of ∼1200 km, which defines the bottoming depths of the direct P- and S-wave arrivals emanating from the furthest events that include a far-side meteoroid impact and a deep moonquake nest (A33). In an attempt to obtain more information on density and the deeper interior (e.g., core size and density), more elaborate approaches to inverting the arrival time data set have been considered. These include adding geodetic and electromagnetic sounding data, use of equation-of-state models, and petrological information (Khan et al. 2007, 2014; Garcia et al. 2011; Matsumoto et al. 2015). While these studies have provided insights on

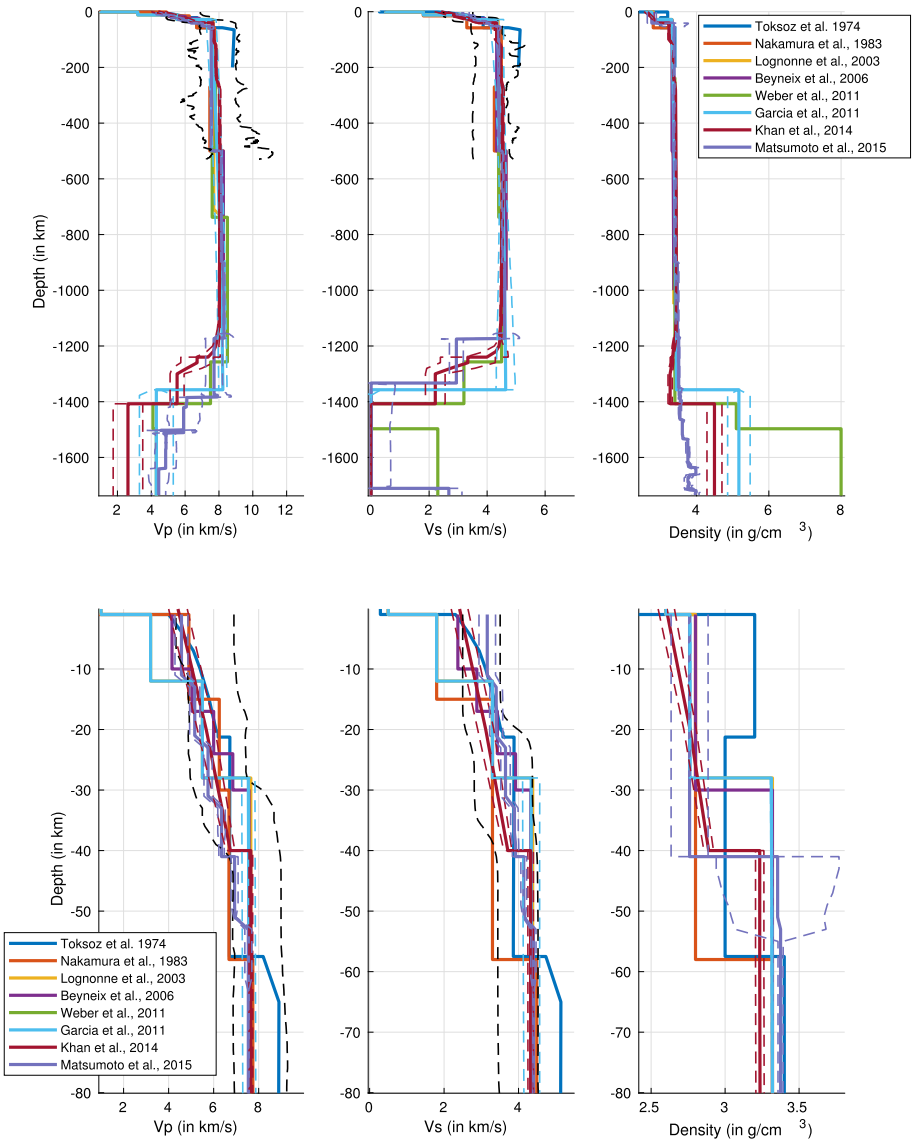

Fig. 4 Comparison of previously published lunar seismic velocity models. Radial profiles of P-wave velocity on the left, S-wave velocity in the center, and density on the right are presented from the surface to center of the Moon (top) and a zoom on crust and uppermost mantle (bottom). Solid lines indicate either mean or most likely model for each study, dashed lines indicate one standard deviation error bar where available. Black dashed lines indicate the contour lines including half of the model distribution with highest probability density in Khan and Mosegaard (2002), limited to the first 500 km of the Moon

the deep lunar interior, particularly mantle density structure, it has proved difficult to tightly constrain core size and density on account of the smallness of the core.

Khan et al. (2006a) computed petrological phase equilibria using Gibbs free energy minimization techniques (Connolly 2009), which were combined with stochastic inversion.

Briefly, stable mineral phases, their modes and physical properties (P-, S-wave velocity and density) were computed as a function of temperature and pressure within the CFMAS system (comprising oxides of the elements CaO, FeO, MgO, Al_2O_3, SiO_2). By inverting the seismic travel time data set of Lognonné et al. (2003) jointly with lunar mass and moment of inertia, while assuming crust and mantle to be compositionally uniform, they determined the compositional range of the oxide elements, thermal state, Mg#, mineralogy, physical structure of the lunar interior, and core size and density.

Garcia et al. (2011) inverted the travel time data of Lognonné et al. (2003) and mass and moment of inertia using the simplified Adams–Williamson equation of state. The latter assumes adiabatic compression of an isochemical material devoid of any mineral phase changes, coupled with a Birch-type linear relationship between seismic velocity and density. Garcia et al. (2011) also considered core reflected phases in an attempt to determine core size. While core reflections were allegedly observed by Garcia et al. (2011) and Weber et al. (2011), it has to be noted that the resultant core size estimates differ largely because of differences in mantle seismic velocities. Garcia et al. (2011) favor a core with a radius of 380 ± 40 km with an outer liquid part, while Weber et al. (2011) find a 150 km thick partially molten mantle layer overlying a 330 km radius core, whose outer 90 km is liquid.

Matsumoto et al. (2015) jointly inverted the travel time data of Lognonné et al. (2003) (event parameters were fixed), mean mass and moment of inertia, and tidal response (k_2 and Q) for models of elastic parameters (shear and bulk modulus), density, and viscosity within a number of layers. Viscosity was included as parameter in connection with a Maxwell viscoelastic model following the approach of Harada et al. (2014). Evidence for a lower mantle low-velocity layer (depth range 1200–1400 km) and a potentially molten or fully liquid core (330 km in radius) was found.

Finally, all available geophysical data and model interpretations are consistent with a Moon that has differentiated into a silicate crust and mantle and an Fe-rich core (e.g., Hood 1986; Hood and Zuber 2000; Wieczorek et al. 2006; Khan et al. 2013). Our current view of

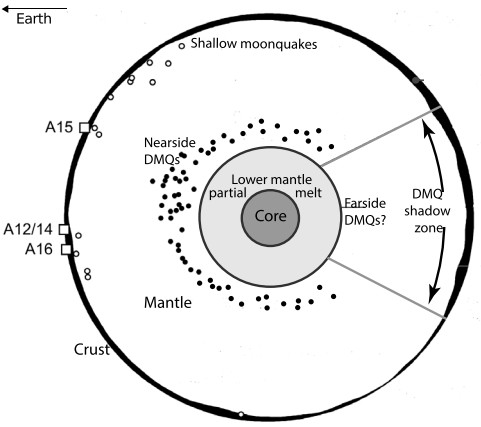

Fig. 5 Schematic diagram of lunar internal structure as seen by a host of geophysical data and models. The Moon has differentiated into crust, mantle, and core with no clear indication for a mid-mantle division, but considerable evidence for a partially molten lower mantle. The core is most likely liquid and made of Fe with a light element (e.g., S or C) with a radius $\lesssim$350 km. Presence of a solid inner core is highly uncertain and therefore not indicated. Apollo stations are indicated by A12–A16 and are all located on the nearside of the Moon. Shallow and deep (DMQ) moonquakes occur in the depth ranges 50–200 km and 800–1100 km, respectively. See main text for more details. Modified from Khan et al. (2014)

the lunar interior is summarised in Fig. 5. Evidence for a mid-mantle dicontinuity separating the mantle into upper and lower parts is uncertain (Nakamura 1983; Khan and Mosegaard 2002), but there is evidence for the presence of partial melt at depth based on analysis of characteristics of farside seismic signals (absence of detectable S-waves) (Nakamura et al. 1973; Sellers 1992; Nakamura 2005) and the long-period tidal response of the Moon (e.g., Williams et al. 2001a; Khan et al. 2004, 2014; Efroimsky 2012b,a; van Kan Parker et al. 2012; Harada et al. 2014). This presence of melt is still debated within the authors of this paper because the above two evidences can also be reproduced by a low viscosity layer not requiring melt (Nimmo et al. 2012). Owing to the distribution of the seismic sources observed on the Moon, the deep interior has been more difficult to image, but the overall evidence suggests that the Moon has a small core with a radius in the range 300–350 km that is most probably either partially or entirely molten (Weber et al. 2011; Garcia et al. 2011). Absence of clear detection of farside deep moonquakes (if located in the deep moonquake shadow zone) seems to support this further (Nakamura 2005). While direct evidence for a solid inner core is highly uncertain, it could be present if a portion of the liquid core has crystallised but will depend crucially on its composition as discussed earlier (Sect. 2.4). Current geophysical constraints on core density estimates do not uniquely constrain composition, but are in favor of a core composed mainly of iron with some additional light elements (e.g., Fei and Brosh 2014; Antonangeli et al. 2015; Shimoyama et al. 2016; Kuskov and Belashchenko 2016; Morard et al. 2018) (see Sect. 2.4). Support for an iron-rich core is also provided by recent measurements of sound velocities of iron alloys at lunar core conditions (e.g., Jing et al. 2014; Nishida et al. 2016; Shimoyama et al. 2016), although the density of these alloys is much higher than those deduced for the core from geophysical data.

4 Seismic Scattering and Attenuation Models

This section summarizes the main findings on the scattering and absorption properties of the Moon. Lunar Q estimates are summarized in Table 3.

4.1 Basic Definitions and Observations

In seismology, attenuation refers to the (exponential) decay of the amplitude of ballistic waves with distance from the source after correction for geometrical spreading and site effects. The two basic mechanisms at the origin of seismic attenuation are energy dissipation caused by anelastic processes and scattering by small-scale heterogeneities of the medium. Each of these mechanisms may be quantified with the aid of a quality factor Q equal to the relative loss of energy of the propagating wave per cycle. In comparison with their terrestrial counterparts, a striking feature of lunar seismograms is the long ringing coda that can last for more than an hour. This is understood as the result of intense scattering in the mega-regolith layer and the extremely low dissipation on the Moon compared to the Earth. Scattering removes energy from the coherent ballistic waves and redistributes it in the form of diffuse waves that compose the seismic signal known as coda. In the case of the Moon, scattering is so strong as to cause a delay of the order of several hundreds of seconds between the onset of the signal and the arrival time of the maximum of the energy. This delay time t_d is a useful characteristics of lunar seismograms and measurements have been reported in several studies (see e.g. Dainty et al. 1974; Gillet et al. 2017). The extreme broadening of lunar seismograms was interpreted by Latham et al. (1970a) as a marker of the diffusion of seismic energy in the lunar interior, a physical model which still prevails today. For this

Table 3 Summary of seismic attenuation estimates in the Moon. The notations ∥ and ⊥ refer to horizontal and vertical diffusivities, respectively. Frequency Dependence (Freq. Dep.) indicates whether the underlying physical model assumes attenuation to be frequency dependent or not. In the study of Nakamura (1976), the first and second value of D refer to the sites of Apollo 15 and Apollo 16, respectively

Reference	Freq. (Hz)	Freq. dep.	Depth range (km)	D (km^2/s)	Dissipation		Observable	Method
					Q_p	Q_s		
Latham et al. (1970a)	1	Yes	<20	2.3–2.5		3600	Seismogram envelope	Diffusion theory
Latham et al. (1970b)	1	Yes	<20			3000	Coda Decay	Diffusion theory?
Dainty et al. (1974)	0.45 1	Yes	<25 <14	∥ 8 ⊥? ∥ 0.9 ⊥ 0.4		5000 5000	Seismogram envelope	Diffusion theory
Dainty et al. (1976a)	1–10	No	0–500 500–600 600–950 950–1200		5000 3500 1400 1100		Average P-wave amplitude	Inter-station spectral ratio
Dainty et al. (1976b)	1–10	No No	<520 520 − 1000		4800 ± 900 1400 ± 300		Average P-wave amplitude	Inter-station spectral ratio
Nakamura et al. (1976)	1–8	No	60–300 300–800		4000 1500		Average P-wave amplitude	Inter-station spectral ratio
Nakamura (1976)	4 5.6 8		<2	2.6×10^{-2}, 3.3×10^{-2} 2.2×10^{-2}, 2.8×10^{-2} 1.8×10^{-2}, 2.2×10^{-2}		1600–1700 1900–2000 2300	Maximum amplitude decay with distance	Diffusion theory for moving sources
Nakamura and Koyama (1982)	1 8	Yes $Q_s \propto f^{0.7\pm1}$	<400		>4000 4000–8000	4000–150000 7000–15000	Average P, S amplitude	Single + inter-station spectral fitting
Simplified from Gillet et al. (2017)	0.5	Yes	0–61 61–95 95–113 113–147 >147	1.9 ± 0.5–8.5 ± 3 16 ± 3–21 ± 5 270 ± 200 365 ± 150–1000 ± 600 4585 ± 2000		2500 ± 25 Id. Id. Id. Id.	Rise time and coda Q of seismogram envelope	Diffusion theory

reason, the strength of scattering in the Moon is most often quantified by a diffusion constant D (expressed in km^2/s) and we shall adhere to this convention (low/high diffusivity corresponding to strong/weak scattering). The notation Q will be employed to denote attenuation due to dissipation processes. The rate of decay of seismograms in the time domain is yet another useful characteristic which may be quantified with the aid of a quality factor, which we shall label Q_c. In the diffusion (multiple scattering) regime, Q_c may be used as proxy for Q in the case of strong stratification of heterogeneity (Aki and Chouet 1975). First attempts to estimate Q from the coda decay were carried out shortly after the deployment of Apollo seismometers. Using data from the artificial impacts, Latham et al. (1970a) and Latham et al. (1970b) found the Q of the upper crust to be in the range 3000–3600. Before discussing these measurements in more detail we briefly review dissipation estimates from lunar rock samples using acoustic sounding.

4.2 Q Measurements of Lunar Samples in the Laboratory

Early experimental measurements of dissipation in lunar rock samples by Kanamori et al. (1970) and Wang et al. (1971) were in sharp contradiction with the first in-situ seismic observations of Latham et al. (1970a,b). Kanamori et al. (1970) and Wang et al. (1971) reported extremely low $Q \approx 10$ at 1 MHz—more than 2 orders of magnitude less than the seismically determined Q—using basic pulse transmission experiments. Besides the low accuracy of these measurements, the very high-frequency at which they were performed questioned the validity of their interpretation in terms of dissipation, since scattering might be efficient around 1 MHz. More accurate estimates by Warren et al. (1971) based on the resonance mode of a vibrating bar around 70 kHz reduced the discrepancy by roughly one order of magnitude, but still left a gap with regard to the seismic observations. The main findings are summarized in Table 4. It should be noted that "Q" may refer to different physical quantities depending on the experimental apparatus (torsion versus vibration). Relations between laboratory Q and seismic Q for both P and S waves are carefully examined in Tittmann et al. (1978).

In a series of papers (see Table 4), Tittmann and co-workers conclusively demonstrated that the large difference between in-situ seismic measurements and their laboratory counterpart could be ascribed to the adsorption of volatiles at the interface of minerals. In particular, infinitesimal quantities of water reduce the Q dramatically so that contamination by laboratory air suffices to hamper attenuation measurements in normal (P, T, humidity) conditions. Tittmann et al. (1975) and Tittmann (1977) showed that intensive degassing by a heating/cool-down treatment dramatically increases the lunar sample Q at both 50 Hz and 20 kHz. Further analyses conducted in an extreme vacuum demonstrated that the very high Q of lunar rocks may be entirely explained by the absence of volatiles in the crust of the Moon.

4.3 Seismic Attenuation Measurements: An Overview of Approaches

Methods Based on the Diffusion Model Scattering and dissipation convey independent information on the propagation medium so that it is valuable to try to evaluate separately the contribution of the two mechanisms. The theory of wave propagation in heterogeneous media shows that separation is indeed possible provided one measures the signal intensity at different offsets between source and station and in different time windows (see Sato et al. 2012, for a comprehensive review). Thus, methods based on the diffusion model have the potential to resolve independently the Q and D structure. This may be achieved by direct

Table 4 Summary of laboratory measurements of dissipation in Lunar rock samples

Reference	Mission	Sample codes	$Q_{p,y}$	$Q_{s,t}$	Method	Environment	Pressure	Temperature	Frequency	Remarks
Kanamori et al. (1970)	Apollo 11	10020/10057/10065	10	10	Amplitude ratio with controlled specimen	Vacuum	200 MPa	Room T.	1 MHz	"At high pressures, all the samples... showed an appreciable increase in Q
Wang et al. (1971)	Apollo 12	12002, 54/12022, 60	15		Amplitude ratio with controlled specimen	Vacuum	$P \approx 0$	Room T.	1 MHz	Samples were dried in 100 degrees oven under vacuum for 2 hours
			17–35		Torsion pendulum	Air	Room P.	Room T.	≈1 Hz	
Warren et al. (1971)	Apollo 12	12063/12038	130–300		Resonance peak half-width	Vacuum Dry nitrogen	≈1.33 Pa ≈0.1 MPa	25°–125 °C	40–130 kHz	"Humidity variation (0–100%) varies Q by factor of 2" "Temperature variation from 25 °C to 125 °C do not change the Q significantly" No difference between $N2$ and vacuum
Tittmann et al. (1972)	Apollo 14	14310,86	10		Resonance peak half-width	Hot water vapor	Room P.	Room T.	Tens of KHz?	"Showed that Q rapidly decreases with water intrusion." "At higher vacuum and lower temperature, Q value increases and approaches what was observed on the Moon"
			50–90			Humid/dry air	Room P.	Room T.		
			130–150			Vacuum	$8e^{-}6$ Pa	Room T.		
			400–800			Vacuum	$8e^{-}6$ Pa	−180 °C		

Table 4 (*Continued*)

Reference	Mission	Sample codes	$Q_{p,y}$	$Q_{s,t}$	Method	Environment	Pressure	Temperature	Frequency	Remarks
Tittmann et al. (1975)	?	70215,85	60		Resonance peak half-width	Lab. air	Room P.	Room T.	20 KHz	
			340			Vacuum	$\approx 1.3 \times 10^{-1}$ Pa	Room T	20 KHz	
			400			Vacuum	$\approx 1.3 \times 10^{-1}$ Pa	Room T	20 KHz	After 1st heating+slow cooling
			800			Vacuum	$\approx 1.3 \times 10^{-1}$ Pa	Room T	20 KHz	After 3rd heating+rapid cooling
			2420			Vacuum	$\approx 1.3 \times 10^{-4}$ Pa	Room T	20 KHz	After 4th heating+rapid cooling
			3130			Vacuum	$\approx 1.3 \times 10^{-5}$ Pa	Room T	20 KHz	After continued pumping
Tittmann et al. (1976)	?	70215,85			Resonance peak half-width	Vacuum	$\approx 1.3 \times 10^{-5}$ Pa	Room T	20 KHz	12 Hrs exposition in vacuum
							$\approx 1.3 \times 10^{-6}$ Pa	Room T	20 KHz	12 Hrs exposition in vacuum
							$\approx 1.3 \times 10^{-8}$ Pa	Room T	20 KHz	14 Hrs exposition in vacuum
Tittmann (1977)	?	70215,85	4882		Resonance peak half-width	Vacuum	$\approx 7 \times 10^{-8}$ Pa	Room T	20 KHz	After intensive outgassing
Tittmann et al. (1978)	?	70215,85	740		Resonance peak half-width	Vacuum	$\approx 1.3 \times 10^{-5}$ Pa	100 °C	20 KHz	All measurements performed after outgassing
			950				$\approx 1.3 \times 10^{-5}$ Pa	50 °C	20 KHz	
			1330				$\approx 1.3 \times 10^{-5}$ Pa	0 °C	20 KHz	
			1430				$\approx 1.3 \times 10^{-5}$ Pa	−50 °C	20 KHz	

modeling of the envelope of signals (Dainty et al. 1974) or by fitting the distance dependence of derived quantities such as the maximum amplitude (Nakamura 1976) or the delay time t_d (Gillet et al. 2017). Because scattering properties depend on the ratio between the wavelength and the correlation length of heterogeneities, analyses are most often performed after application of a narrow band-pass filter and shed light on the frequency dependence of the attenuation properties. The neglect of the coherent (or ballistic) propagation, however, is a strong limitation of the diffusion approach. While both diffusivity and seismic Q depend linearly on the individual scattering and absorption properties of P and S waves, diffusion considers the transport of the total, i.e., kinetic and potential, energy only and cannot resolve the contribution of the different propagation modes. It is worth pointing out that multiple scattering results in an equipartition of energy among all propagating modes so that the typical ratio between the S and P energy density is given by $2(V_p/V_s)^3$. Therefore the Q and D deduced from the diffusion model are mostly representative of the properties of S waves.

Spectral Ratio Technique Another approach to the measurement of attenuation is based on the decay of the typical amplitude of direct P- and S-waves as a function of hypocentral distance. In short-period terrestrial seismology, this is most often performed by averaging the amplitude in a time window of a few seconds around the direct arrivals (P or S). The measurement is subsequently corrected for source and site effect by the coda normalization method (Sato et al. 2012). A linear regression of the data in the distance—log(amplitude) plane yields an estimate for Q. In this case only an apparent Q combining effects of scattering and absorption can be retrieved. The lunar case presents a more complicated case because the distance between stations is too large to apply coda normalization. As a remedy, some authors like Nakamura and Koyama (1982) advocate the use of the median of the amplitudes measured on a set of events to normalize the data. Furthermore, scattering on the Moon is so strong, particularly in the first tens of kilometers (see below), that it is necessary to compute the mean amplitude of the P or S wave train over a long time window (1 or 2 minutes) to average out signal fluctuations. Intuition suggests that this procedure somehow "corrects" for the strong broadening of the signal caused by multiple scattering so that it may be expected that the so-retrieved Q mostly reflects dissipation properties. When few stations are available, as on the Moon, it is also preferable to use spectral ratios between pairs of stations (rather than decay with distance) and to perform a regression of the decay of the amplitude ratio in the frequency domain. In simple stratified models, the attenuation estimated in this two-station approach may be ascribed to the depth interval where the rays do not overlap. This method however implicitly requires that attenuation be frequency independent, which is a severe limitation. This difficulty has been overcome by Nakamura and Koyama (1982) who developed a rather sophisticated method employing both single and two-stations measurements.

4.4 Estimates of Diffusivity (D) and Dissipation (Q)

Results of Diffusion Modeling Latham et al. (1970a,b) fitted seismogram envelopes with a diffusion model in Cartesian geometry to estimate Q (≈ 3000) and D (≈ 2.5 km^2/s) at 1 Hz in the upper crust of the Moon.

Dainty et al. (1974) pointed out that the delay time of the maximum t_d seemed to plateau beyond 170 km distance from the source. They interpreted this observation as a signature of heterogeneity stratification in the Moon and proposed that the first ten km of the Moon would be highly scattering while the underlying medium would be transparent. Based on envelope

fitting, they re-evaluated the diffusivity and Q at two different frequencies (see Table 3). Dainty et al. (1974) found significantly higher Q than previous authors. They explained the difference by the fact that part of the decay of the coda originated structurally: the energy that leaks out of the scattering layer is an apparent loss so that the Q estimated from coda decay tends to overestimate effects of dissipation. While the explanation of Dainty et al. (1974) is reasonable, their model was designed in Cartesian geometry so that no energy would be able to re-enter the scattering layer.

Gillet et al. (2017) has extended this "refraction" of diffuse waves to spherical geometry and showed it to be the key process in explaining the non-monotonous dependence of the delay time t_d on epicentral distance. Using global t_d measurements, Gillet et al. (2017) confirmed the existence of a strong stratification of heterogeneity and found that scattering would be efficient up to a depth of roughly 100 km, which would correspond to the base of the mega-regolith. Their analysis showed no evidence for stratification of Q.

Nakamura (1976) used the lunar rover as an active seismic source to study the diffusion and dissipation of energy in the uppermost crust of the Moon. This method uses the difference of maximum amplitude for sources approaching or receding from the seismic stations, respectively. He performed observations around 4 Hz, 5.6 Hz and 8 Hz to study the frequency dependency of Q and D (see Table 3 for details). Within the studied areas, near Apollo stations 15 and 16, no significant regional differences were detected. Although the measurements were not performed in the same frequency band, the values of Q and D reported by Nakamura (1976) are much lower than those found by Gillet et al. (2017). This suggests the existence of a strong depth dependence of D and Q in the first kilometer of the Moon.

Results of the Spectral Ratio Method With the exception of the work of Nakamura and Koyama (1982), the spectral ratio method only gives access to an average value of attenuation in a given frequency band. It has the potential, however, to distinguish between Q_p and Q_s and to constrain the attenuation at greater depth than the diffusion method (which is likely limited to the first 150 km of the Moon). An important outcome of attenuation studies based on the spectral ratio approach is that the data require a stratified Q in the mantle.

By studying events with different penetration depths, Dainty et al. (1976a) concluded that the upper 500 km has Q_p values as high as 5000 and then decreases with depth. They suggest Q_p values of, respectively, 3500, 1400 and 1100 for the depth intervals 500–600 km, 600–950 km and 950–1200 km. Dainty et al. (1976b) reported similar Q_p values (1400 ± 300 above 520 km depth and 4800 ± 900 below), but note that their estimation is not reliable below 1000 km. A similar decrease of Q_p with depth was also reported by Nakamura et al. (1976), who studied the ratio of amplitude variations with epicentral distance at two different frequencies (1 Hz and 8 Hz). Using amplitude variations in the epicentral distance range 40°–90°, they obtained $Q \approx 4000$, which they regarded as representative of the upper mantle. From the data at 110°–120° epicentral distance, they found $Q \approx 1500$, confirming the observation that mantle Q_p appears to decrease with depth.

Finally, Nakamura and Koyama (1982) used spectra of records from shallow moonquakes from 3 Hz to 8 Hz to study the frequency dependence of the seismic Q for both P and S waves. They focused on events in the 30°–90° epicentral distance range, corresponding to rays bottoming in the upper mantle. In spite of large uncertainties regarding geometrical spreading, the results showed that Q_P should be greater than 4000 at 3 Hz and between 4000–8000 at 8 Hz. This frequency dependence, however, is not deemed significant since it resides within error bars. On the other hand, possible values for Q_S are 4000–15000 at 3 Hz and 7000–1500 at 8 Hz. This frequency dependence can be considered significant and may be summarized as $Q_S \propto f^{0.7 \pm 0.1}$.

4.5 Future Work

In summary, the mantle of the Moon is most probably highly transparent, so that diffusion theory does a poor job at modeling the energy propagation at depth. On the other hand, interpretation of results from the spectral ratio technique is complicated by the coupling of modes that occurs upon scattering. Both the diffusion and spectral ratio technique have merits so that a method that would facilitate the simultaneous analysis of direct and scattered wave trains would be desirable. Radiative transfer (Margerin and Nolet 2003) or simulations based on the Monte Carlo method (Blanchette-Guertin et al. 2015) are both promising methods.

5 Seismic Source Locations

To infer a velocity model requires accurate location of all seismic sources. For all naturally occurring events, i.e., meteoroid impacts and shallow and deep moonquakes, events parameters need to be determined before or with the structural parameters from the lunar seismic arrival time data set. Such inversions, however, can be affected by trade-offs between source location and velocity model. A compilation of determined epicentral locations based on both Apollo-era and recent studies are shown in Fig. 6. Errors on locations are generally large, reflecting discrepant data analysis and inversion methods. Hempel et al. (2012) also showed that the small-aperture Apollo network limited the accuracy with which many deep moonquake nests could be located (Fig. 7). The characteristics of the various events are discussed in detail in the companion paper (Sect. 3). Here, we only discuss various location estimates.

Oberst (1989) obtained the locations of 18 large meteoroid impact events by compiling a set of arrival time measurements based on own work and earlier measurements by Goins (1978) and Horvath (1979). The large events were then used as "master events" to establish the relationship between the distances, amplitudes, and rise times of the meteoroid impact signals. Relying on these empirical relationships, locations and magnitudes of 73 smaller meteoroid impacts were estimated by Oberst (1989). Most of the located small events were found to have occurred around the stations. Subsequent reprocessing of the data by Lognonné et al. (2003) resulted in the detection of 19 meteoroid impact events, which were relocated by Garcia et al. (2006) and Garcia et al. (2011) and are shown in Fig. 6b. In the 8 years of seismic monitoring, about 1730 impacts were detected (Nakamura et al. 1982).

The rarer shallow moonquakes (28 in total, with an average 5 events per year) were first identified as high-frequency teleseismic (HFT) events (Nakamura et al. 1974). Although rare (Nakamura et al. 1976), their large amplitude, strong shear-wave arrival, and unusually high frequency content make these events distinct from the other type of sources. While clearly of internal origin, it has proved challenging to determine source depth from first-arrival time readings. Nakamura et al. (1979) examined the variation of the amplitude with distance, which suggested that the shallow moonquakes occur in the upper mantle of the Moon. Assuming a source depth of 100 km, Nakamura et al. (1979) attempted to establish a possible link between the shallow moonquakes with lunar impact basins. While not conclusive, source depths around 100 km seemed reasonable given the available evidence. Although uncertainties remain large, subsequent arrival time inversions generally confirm this observation with HFT source depths constrained to 50–200 km (Lognonné et al. 2003; Garcia et al. 2006, 2011; Gagnepain-Beyneix et al. 2006; Khan and Mosegaard 2002) (Fig. 6c).

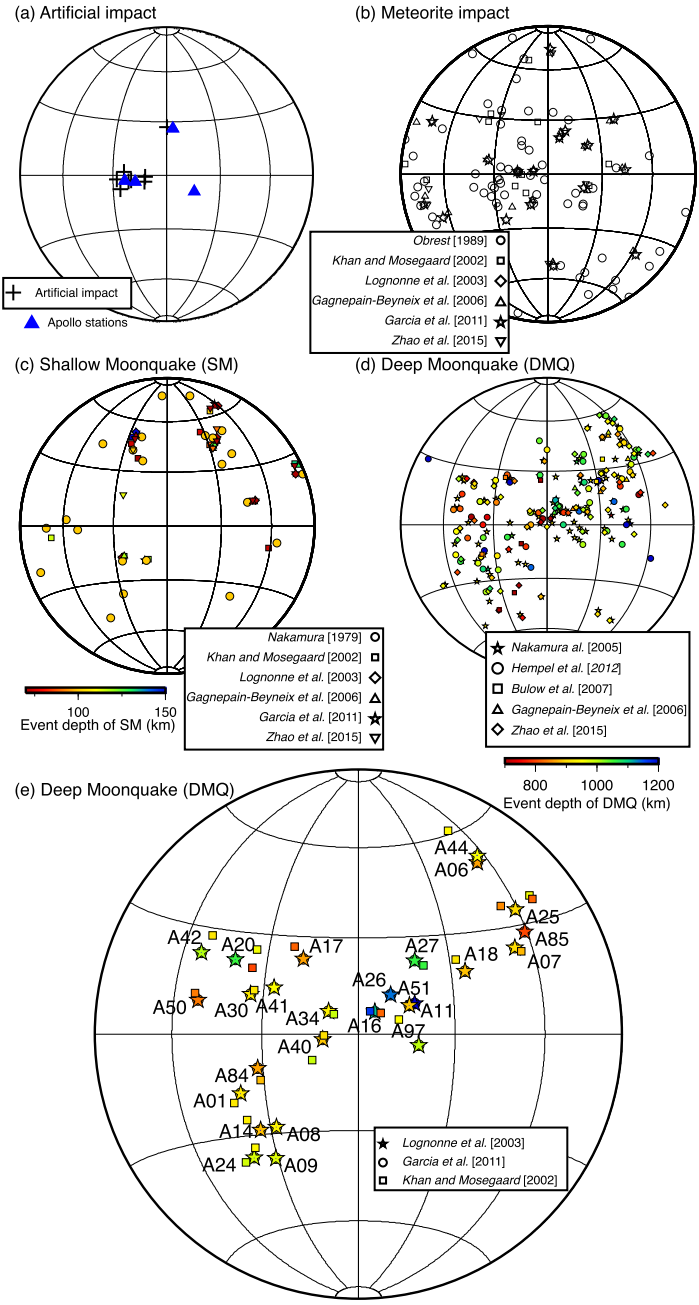

Fig. 6 Locations of impacts and moonquakes on the lunar nearside. The locations of (**a**) artificial impacts, (**b**) meteoroid impacts, (**c**) shallow moonquakes, (**d**) and (**e**) deep moonquakes from different studies are displayed. The locations of artificial impacts are from Garcia et al. (2011). The blue triangles in (a) represent the locations of the four Apollo seismic stations. Note that the event depths of shallow mooquakes in Nakamura et al. (1979) were fixed to 100 km. (**d**)–(**e**) display the source locations of the DMQ's from different studies. The color denotes event depth. Note the location of Hempel et al. (2012) in (d) is the centroid of location cloud instead of an absolute location, which is resolved in other studies

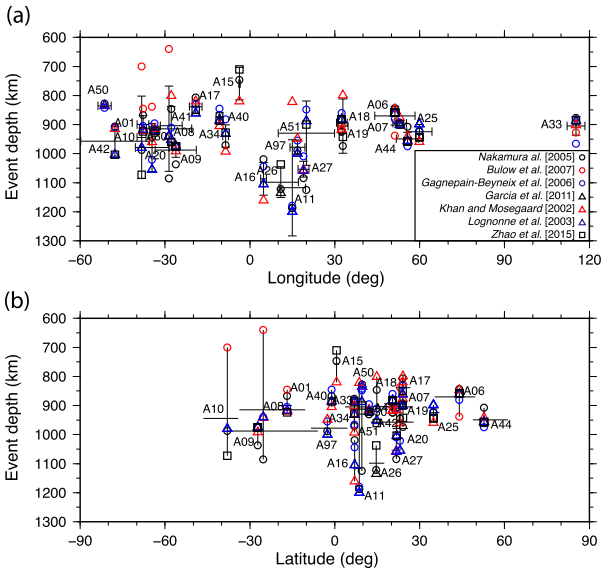

Fig. 7 Variations of the locations of the deep moonquakes (DMQ's) from different studies. (**a**) displays the mean and standard deviation of DMQ hypocentral coordinates based on different studies (see main text and Fig. 6 for details). (**b**) displays the mean and range of DMQ locations. Only DMQ clusters for which at least three studies provide locations are reported are plotted here. To emphasize the depth variation, individual DMQ locations from different studies are plotted using different symbols with varied depths using same (a) mean longitude and (b) mean latitude

By modeling the attenuation properties of short-period body waves that are generated by the shallow moonquakes, Gillet et al. (2017) concluded that HFTs are confined to the depth range 50 ± 20 km, which suggests brittle failure of deep faults as possible origin. Frohlich and Nakamura (2006) have also invoked strange quark matter as a possible source of HFTs, based on the observation that essentially all of the 28 shallow moonquakes occurred when the Moon was facing a certain direction relative to stars. This implies that the HFT events could be either caused or triggered by unknown objects that originates extraneous to the solar system.

The most numerous signals recorded by the seismic network were the deep moonquakes (DMQs). A particular feature of the DMQs is that they are clustered in discrete regions (nests). Stacking events from the same nest enhances signal-to-noise ratio and therefore picking accuracy even in the case of small-amplitude seismic signals, as a result of which picks are generally made on stacked DMQ waveforms. Location errors are typically large and different studies show significant discrepancy (Fig. 6d–e and Fig. 7), which reflects differences in underlying assumptions and modeling aspects (Lognonné et al. 2003; Garcia et al. 2011; Gagnepain-Beyneix et al. 2006; Khan and Mosegaard 2002; Zhao et al. 2015). More details on DMQ analysis and characteristics is provided in our companion paper (Nunn et al. submitted).

6 Seismic Model Inversions

In view of the re-compiled Apollo lunar seismic arrival time data set (Nunn et al. submitted) and the latest a priori assumptions described earlier, we re-assess interior structure. For this purpose, we consider three independent parameterisations and inversion methods. The goal here is not to produce a single model, but rather a family of models that fit the data and are consistent with the most recent set of prior constraints. Although we make the simplifying assumption of keeping source parameters fixed, this approach will allow us to identify

Table 5 Summary of lunar geodetic data parameters and uncertainties used in the inversions

Variable	Value	Source
Mass	$7.34630 \pm 0.00088 \times 10^{22}$ kg	(Williams et al. 2014)
R	1737.151 km (1737.151 km)	(Wieczorek 2015)
I_s/MR^2	0.393112 ± 0.000012	(Williams and Boggs 2015)
k_2: elastic, $\alpha = 0.3$	0.02294 ± 0.00018	Sect. 2.1 this study
k_2: elastic, $\alpha = 0.1$–0.4	0.02248 ± 0.00072	Sect. 2.1 this study
h_2 (LLR): elastic, $\alpha = 0.3$	0.0450 ± 0.0058	Sect. 2.1 this study
h_2 (LLR): elastic, $\alpha = 0.1$–0.4	0.0441 ± 0.0058	Sect. 2.1 this study
h_2 (LOLA): elastic, $\alpha = 0.3$	0.0353 ± 0.0031	Sect. 2.1 this study
h_2 (LOLA): elastic, $\alpha = 0.1$–0.4	0.0346 ± 0.0033	Sect. 2.1 this study

similarities and discrepancies among the various internal structure models in order to determine properly resolved structures. We consider three parameterisations and inversions based on the previous work of Drilleau et al. (2013), Garcia et al. (2011), and Khan et al. (2014). These studies span a relatively wide range in terms of model parameterisation from the "standard" seismic parameterisation (model 1), to a simplified equation-of-state method (model 2) over a fully self-consistent thermodynamic method (model 3) that allows for the computation of petrologic phase equilibria and seismic properties. As for the inversions, we consider a two-pronged approach that involves both model inversion (models 1 and 2) and model assessment (model 3). Models based on parameterisations 1 and 2 are obtained from inversion of the lunar seismic travel time data set, whereas models relying on parameterisation 3 are only used in a predictive sense, i.e., models obtained from inversion of electromagnetic sounding (Table 6) and geodetic data (k_2, M, and I/MR^2) are employed to predict P- and S-wave travel times that are subsequently compared to observations. While the fit to the travel time data for this particular set of models will evidently be less than for the other models, this predictive exercise is nevertheless important as it assesses to (1) what extent the different geophysical data sets are compatible; (2) the reliability of the underlying parameterisation to simultaneously fit geophysical data sets that are sensitive to distinct physical properties (e.g., seismic wave speeds, density, electrical conductivity). The forward modeling scheme, i.e., mapping from model structure to travel times, relies in all three cases on a ray-theoretical approach to compute body wave travel times. The specific data used in the inversion are the median P and S arrival times compiled in our companion paper for M1 and M2, and the latest geodetic observations (k_2, h_2, M, and I/MR^2) (for $\alpha = 0.3$) compiled in Table 5 for M2 and M3, with the simplifying assumption that the solid-body mean moment of inertia (I_s) is equal to that of the entire body. Common to all three models are assumptions of a spherically symmetric body.

6.1 Model Parameterisation and Prior Information

6.1.1 Model 1

The models are parameterized with Bézier points, which are interpolated using polynomial C_1 Bézier curves. The advantages of this parameterisation is that it relies on a small number of parameters (Bézier points) and it does not impose a regularly spaced discretization of the models or prior constraints on layer thicknesses and location of seismic discontinuities. It

Table 6 Observed apparent resistivity (ρ_a) and error ($d\rho_a$) calculated from Apollo lunar day-side transfer functions (Hobbs et al. 1983)

Period (s)	ρ_a (Ωm)	$d\rho_a$ (Ωm)
100000.00	58.6	2.1
50000.00	113.9	4.0
33333.33	164.5	5.7
25000.00	209.8	7.4
20000.00	250.8	9.2
16666.67	288.7	11.0
14285.71	324.6	12.7
12500.00	358.9	13.9
11111.11	392.3	14.4
10000.00	424.8	14.2
5000.00	693.5	36.6
3333.33	921.4	70.5
2500.00	1099.2	91.9
2000.00	1212.7	109.6
1666.67	1283.2	110.8
1428.57	1350.8	96.8
1250.00	1471.7	82.3
1111.11	1542.5	74.5
1000.00	1674.9	84.3

Table 7 Data sets and prior information of internal structure model inversions. ISSI team seismological data sets and quake locations are summarized in our companion paper (Nunn et al. submitted)

Model name	M1	M2	M3
Data / prior			
Body wave travel times	ISSI team data set	ISSI team data set	ISSI team data set (prediction)
Electromag. sounding	None	None	Table 6
Geodetic data	None	Table 5	Khan et al. (2014)
Prior source locations	ISSI team compilation	ISSI team compilation	ISSI team compilation

can be used to describe both a gradient and a sharp interface with a minimum of parameters (the reader is referred to Drilleau et al. 2013 for more details). The inverted parameters are the 2 vectors corresponding to the Bézier points for V_P, and the depth at which these Bézier points are located. The Bézier points are randomly located in depth within the prior range (see Table 8). The model parameter vector contains 15 points with the last point located at the core-mantle-boundary (CMB). The depth to the CMB is allowed to vary between 1200 and 1400 km depth. In order to estimate V_S, the V_P/V_S ratio profile is also inverted for using 4 Bézier points that are randomly sampled between 1.5 and 2.2. Note that density is not inverted for with this approach. For the core, we assume that it is entirely liquid and homogeneous, as a consequence of which $V_S = 0$ km/s and V_P is randomly sampled between 0.5 and 9.5 km/s. To account for local differences beneath stations, P- and S-wave station corrections are considered by adding to the computed P- and S-wave travel times, for a given model, a value randomly sampled between -4 and 4 s.

Table 8 Summary of M1 model parameters and model parameter ranges (prior information)

Description	Quantity	Parameter	Value/Range	Distribution
V_p between surface and core	15		0.5–9.5 km/s	uniform
V_p/V_s ratio between surface and core	4		1.5–2.2	uniform
Core/mantle boundary depth	1		1200–1400 km	uniform
Core V_p	1		0.5–9.5 km/s	uniform
Core V_s	1		0 km/s	fixed
P-wave station corrections	4	T_{corP}	−4–4 s	inverted from travel times
S-wave station corrections	4	T_{corS}	−4–4 s	inverted from travel times

To compute body wave travel times, we rely on the ray tracing algorithm of Shearer (2009). To solve the inverse problem, we employ a Markov chain Monte Carlo approach (Mosegaard and Tarantola 1995). This technique allows us to sample a large range of models and provides a quantitative measure of model uncertainty and non-uniqueness. Prior information on model parameters is summarised in Table 8.

6.1.2 Model 2

This parameterisation is an improved version of the parameterisation used by Garcia et al. (2011). The crust is fixed in terms of velocity and density, but the average crustal thickness is a free parameter.

The seismic/density model of the mantle is separated into two parts: a lithosphere which covers the region from the crust-mantle boundary to radius R_L in which the thermal gradient ($(\frac{dT}{dz})_{OA}$) is assumed to be constant, and an adiabatic part from radius R_L to the CMB (radius R_{CMB}).

In the lithosphere, the seismic/density model follows the modified Adams–Williamson equation (Stacey and Davis 2008):

$$\frac{d\rho}{dz} = \frac{\rho g}{\phi} - \alpha\rho\tau \tag{1}$$

where ρ is density, z is depth, g is gravitational acceleration, $\phi = \frac{K_T}{\rho} = V_P^2 - \frac{4}{3}V_S^2$ the seismic parameter, K_T is incompressibility, α is thermal expansion and τ is the super adiabatic gradient. This last term is defined by the following equation:

$$\tau = \frac{dT}{dz} - \left(\frac{dT}{dz}\right)_{adiabatic} = \left(\frac{dT}{dz}\right)_{OA} \tag{2}$$

in which the adiabatic gradient is defined by: $(\frac{dT}{dz})_{adiabatic} = -\frac{g}{\alpha\phi}$.

The Adams–Williamson equation assumes an adiabatic gradient, and consequently, $\tau = 0$. Given lunar mass, or equivalently surface gravity acceleration, and the seismic velocity model, the Adams–Williamson equation is integrated from top to bottom to compute density. To compute V_P from the density model, we employ Birch's law with constant parameters (a and b) over the mantle. The $\frac{V_P}{V_S}$ ratio profile is inverted with three reference points at the top and bottom of the mantle and at 700 km radius. This parameter is linearly interpolated in between these reference points and used to determine V_S.

However, in the lithosphere where thermal gradients are likely super adiabatic, the integration of (1) requires the knowledge of both τ and α. Our model parameterisation assumes

that $\tau = (\frac{dT}{dz})_{OA}$ is constant in the lithosphere. However, thermal expansion α varies with pressure, temperature, and density. We take two important assumptions. First we assume that the product $\alpha \cdot K_T$ is constant over the whole mantle and equal to $4.0 \cdot 10^6 \pm 0.8 \cdot 10^6$ MPa/K (Stixrude and Lithgow-Bertelloni 2005). Next, we assume that the gruneisen parameter is also constant for the whole mantle and equal to $\gamma_{th} = 1.2 \pm 0.2$ (Poirier 2000). Finally, knowing seismic velocities, and consequently the adiabatic incompressibility K_S and temperature, we can use a set of well-known thermodynamic relations to estimate α through the following relation (Poirier 2000):

$$\alpha = \frac{(\alpha K_T)}{K_S - \gamma_{th} \cdot (\alpha K_T) \cdot T} \tag{3}$$

where T is temperature. This formulation imposes the computation of the absolute temperature, whereas up to now only temperature gradients in the mantle were needed. To scale our mantle temperature model we will assume arbitrarily that the temperature at the crust-mantle boundary is equal to 300 K. Error analysis suggests that the error on α so estimated is dominated by the error of the product $\alpha \cdot K_T$ (20%) even in the case of large errors ($\sim$300 K) on absolute temperatures. Once thermal expansion has been computed, equation (1) can be integrated with Birch's law and $\frac{V_P}{V_S}$ ratio to construct seismic and thermal profiles of the lithosphere. The same method is applied to the adiabatic part at the bottom of the mantle with $\tau = 0.0$. The core is parameterized using an average radius and density. Constant values for P and S wave velocities are fixed to 4.0 km/s and 0.0 km/s, respectively, to allow for the computation of Love numbers. The effect of core properties have little influence on the Love numbers because of the small size of the core. Core density will be deduced from the rest of the model parameters by fitting lunar mass and moment of inertia.

Model parameters are summarized in Table 9. The inversion is performed by building lunar models (seismic velocity and density profiles) from random values of the inverted parameters. Then, only lunar models predicting geodetic variables within their error bars are selected (see Table 5). A first set of 30 lunar models for each core radii (sampled by 5 km steps from 250 to 550 km radius) are selected. For each of these models station correction parameters (T_{corP} and T_{corS}) are inverted to minimize the cost function of seismic travel times. Then, the parameter space is explored using the Neighbourhood Algorithm (Sambridge 1999) at each core radius, always imposing that the selected models predict geodetic variables within their error bars, and inverting for station correction parameters. The Neighbourhood Algorithm is performed with 16 loops exploring the neighbourhood of the 3 best models of the parameter space with 10 new models. The whole ensemble of models explored is considered, and only 1% of the models with the best cost function are kept for the ensemble analysis.

6.1.3 Model 3

The composition of the lunar mantle is investigated using the model chemical system CaO–FeO–MgO–Al_2O_3–SiO_2–TiO_2 (CFMASTi). We assume that mantle mineralogy is dictated by equilibrium and compute this from thermodynamic data as a function of pressure, temperature, and bulk composition by Gibbs energy minimization (Connolly 2009). For these calculations, we consider the stoichiometric solid phases and species in the thermodynamic data compilation of Holland and Powell (1998, revised 2002) together with the silicate melt and non-stoichiometric phases summarized in Table 2 of Khan et al. (2014). The silicate melt model is based on pMELTS (Ghiorso et al. 2002). Thermodynamic properties are computed

Table 9 Summary of M2 model parameters and model parameter ranges (prior information)

Description	Quantity	Parameter	Value/Range	Distribution
Crust density	1		2600 kg/m^3	fixed
Crust seismic model	NA	LG03	fixed	
Crustal thickness	1		30–45 km	uniform
Density Jump at crust-mantle boundary	1		400–00 kg/m^3	uniform
Base of lithosphere radius	1		600–1630 km	uniform
Excess thermal gradient in lithosphere	1	0–10 K/km	uniform	
Birch law parameter "a" (mantle)	1	a	−13–−5 km/s	uniform
Birch law parameter "b" (mantle)	1	b	3–7	uniform
V_p/V_s ratio at top of mantle	1		1.65–1.85	uniform
V_p/V_s ratio at 700 km radius	1		1.65–1.85	uniform
V_p/V_s ratio at bottom of mantle	1		1.65–1.85	uniform
Core radius	1		250–550 km	uniform
Core V_p	1		4.0 km/s	fixed
Core density	1		3000–8000 kg/m^3	deduced from Mass budget
P-wave station corrections	4	T_{corP}	−10–10 s	inverted from travel times
S-wave station corrections	4	T_{corS}	−10–10 s	inverted from travel times

for the aggregate at the temperature of interest. To determine elastic moduli the Hashin–Shtrikman bounds are averaged.

For this particular model, we assume that the Moon is divided into a number of layers that constitute crust, upper and lower mantle, and core. Crustal composition (c_{cr}) is fixed to that of Taylor et al. (2006) with temperature T and constant thickness d_1. To better capture variations in crustal properties (ρ, P- and S-wave speed), we employ a function of the form $f_i' = f_i \cdot \phi$, where f_i is one of the aforementioned physical properties in crustal layer i computed thermodynamically and ϕ is a depth-dependent porosity parameter based on the results from GRAIL (Wieczorek et al. 2013). The mantle is divided into two layers that are parameterized by thicknesses d_2 and d_3, compositions X_2 and X_3 and temperature T. Mantle compositions are uniform in each layer and temperature is defined at a number of fixed radial nodes. The physical properties of the core are specified by radius (r_{c}), density (ρ_{c}), and electrical conductivity (σ_{c}), respectively. Model parameterisation is illustrated in Fig. 8 and prior information is summarised in Table 10.

Once all the model parameters values have been assigned, we can compute radial profiles of equilibrium modal mineralogy, seismic properties, and electrical conductivity as a

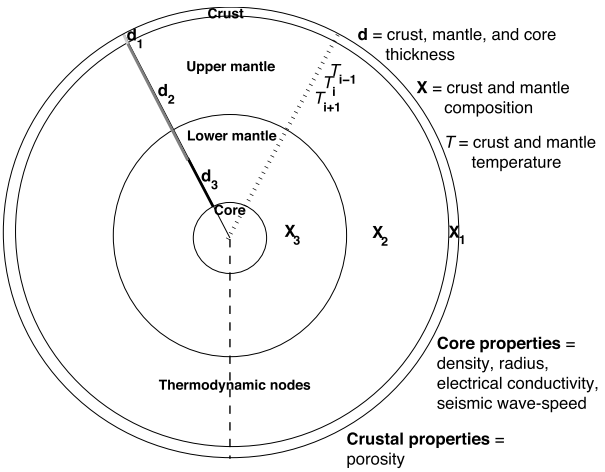

Fig. 8 Model 3 parameterisation

Table 10 Summary of M3 model parameters and model parameter ranges (prior information)

Description	Quantity	Parameter	Value/Range	Distribution
Surface porosity	5	ϕ	0.4–0.75	uniform
Surface temperature	1	T_{surf}	0 °C	fixed
Crustal thickness	1	d_1	40 km	fixed
Upper mantle thickness	1	d_2	$d_1 < d_2 < d_3$	uniform
Lower mantle thickness	1	d_3	$d_2 < d_3 <$ 1737.151 km-r$_{core}$	uniform
Crustal composition (in the NCFMAS system)	5	X_1	Taylor et al. (2006) values given in Table caption	fixed
Upper mantle composition (in the NCFMASTi system)	5	X_2	variable	uniform
Lower mantle composition (in the NCFMASTi system)	5	X_3	variable	uniform
Temperature	40	T_{i}	variable	$T_{i-1} < T_i < T_{i+1}$
Core radius	1	r_{core}	0–434 km	uniform
Core density	1	ρ_{core}	ρ_m–7.5 g/cm^3	uniform
Core S-wave speed	1	V_S^{core}	0 km/s	fixed
Core P-wave speed	1	V_P^{core}	2–5 km/s	variable
Core electrical conductivity	1	σ_{core}	10^5 S/m	fixed

function of pressure, temperature, and composition at intervals of 20 km (thermodynamic nodes) from the surface to the core-mantle-boundary. Since electrical conductivity is less important in the context of computing seismic travel times, we skip the details of how bulk electrical conductivity profiles (shown in Fig. 2a) are determined and refer the interested reader to Khan et al. (2014).

6.2 Definition of Cost Function

We use the following L_1 norm-based cost function

$$J_1 = \sum_{N_p} \frac{|T_p^{obs} - T_p^{calc}|}{\sigma_p} \sum_{N_s} \frac{|T_s^{obs} - T_s^{calc}|}{\sigma_s} \tag{4}$$

$$J_2 = \frac{|M^{obs} - M^{calc}|}{\sigma_M} + \frac{|C^{obs} - C^{calc}|}{\sigma_c} \tag{5}$$

$$J_3 = \frac{|k_2^{obs} - k_2^{calc}|}{\sigma_{k_2}} + \frac{|h_2^{obs} - h_2^{calc}|}{\sigma_{h_2}} \tag{6}$$

$$J_4 = \sum_{\omega} \frac{|\rho_a^{obs}(\omega) - \rho_a^{calc}(\omega)|}{\sigma_{\rho_a}} \tag{7}$$

where the first cost function (J_1) computes the misfit between the number of observed (N_p, N_s) and computed P (T_p) and S (T_s) wave travel times within error bars (σ_p and σ_s) (see Fig. 11 of Nunn et al. submitted). The second and third cost functions (J_2 and J_3) determine fits to mean mass (M) and mean moment of inertia ($C = I/MR^2$), degree-2 Love numbers determining gravity (k_2) and shape (h_2) responses, respectively, within error bars σ_k, where k refers to either M, I/MR^2, k_2 or h_2 (Table 5). The fourth cost function (J_4) determines the fit to electromagnetic sounding data within errors σ_{ρ_a} (Table 6). Superscripts throughout refer to observations (obs) and computed data (calc). Due to the differing model parameterisations, model suite 1 (M1) only minimizes J_1, whereas model suite 2 (M2) minimizes $J_1 + J_2 + J_3$ and model suite 3 (M3) minimizes $J_2 + J_3 + J_4$ while computing J_1 in a predictive sense. Inversion output consists of ensembles of internal structure models that fit the cost functions.

6.3 Inversion Results and Discussion

Results from the inversions in the form of median profiles of V_P, V_S, and ρ, including mean absolute deviation, are shown in Fig. 9. For comparison, some recent models discussed in Sect. 3 are also shown. For further use, median models are compiled in Appendix A.1 and Table 11. Misfit values and computed P- and S-wave travel times for the three models are shown in Fig. 10 and 11, respectively.

By comparing the three models, the following observations can be made:

1. Crustal structure differs between the three models and reflects the different prior constraints employed: M1: variable crustal thickness without imposing a crust-mantle discontinuity; M2: variable crustal thickness with an imposed crust-mantle discontinuity; and M3: fixed crust-mantle discontinuity at 40 km depth.
2. In the uppermost mantle (depth range 60–200 km), models M1 and M2 are in good agreement and suggest the presence of a low-velocity layer (LVL). The extent of this layer differs between the two models, which possibly relates to their different crustal structures. An indication of the presence of a LVL in the upper mantle was first noted from the difference in arrival times from shallow moonquakes compared with those from deep moonquakes and meteoroid impacts (Nakamura et al. 1974). Khan et al. (2006a) also found a decrease in V_S with depth owing to the enhanced effect of temperature on V_S over that of pressure. There is less overlap between M1 and M2 in the mid-mantle (depth range

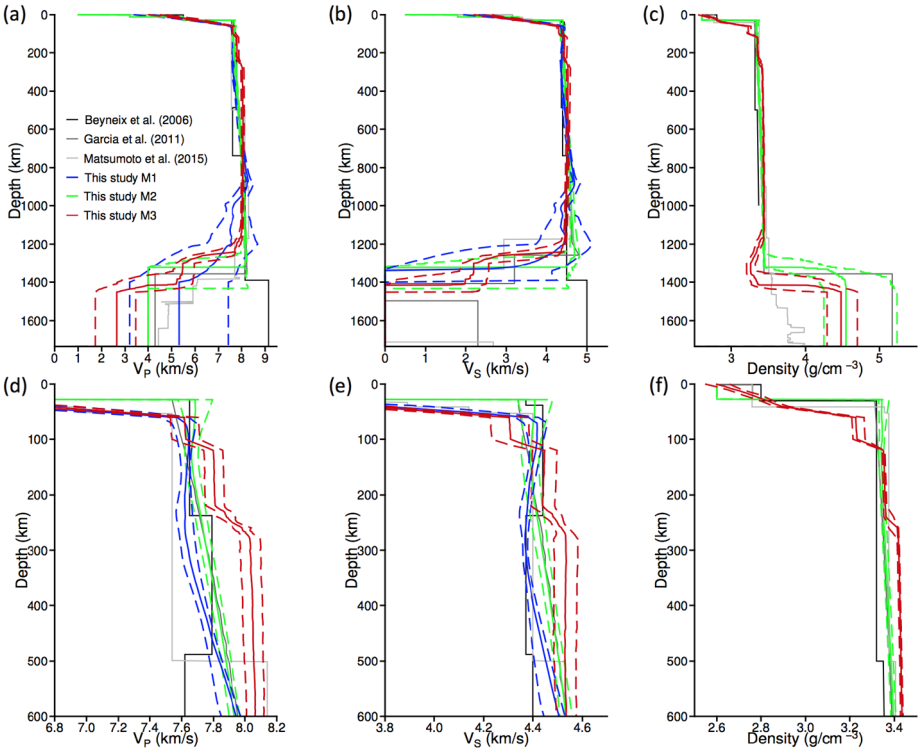

Fig. 9 Comparison of previously published lunar internal structure models with model suites M1, M2, and M3. Radial profiles of P-wave velocity (**a**), and S-wave velocity (**b**), and density (**c**) as a function of depth. Plots in the bottom panel (**d**–**f**) show a zoom on upper mantle structure. Solid and dashed lines show median profiles ± mean absolute deviation obtained from all sampled models

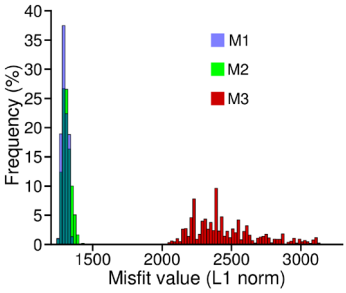

Fig. 10 Distributions of misfit (L_1) values for model suites M1, M2, and M3. Misfit values are based on the "seismic" cost function J_1 (Eq. (4)). Model parameterisations are described in Sect. 6.1

200–500 km). Model M3 differs throughout this depth range with significantly higher seismic P-wave speeds but moderately overlapping S-wave speeds (in the depth range 100–250 km). These differences between M1/M2 and M3 are also discernable from the travel time residuals plotted in Fig. 11, where a positive trend for P-waves in the 25°–80° epicentral distance range is apparent for M3, but less so for M1 and M2. This difference between M1/M2 and M3 suggests that the seismic data constrain the first 600 km of the lunar interior.

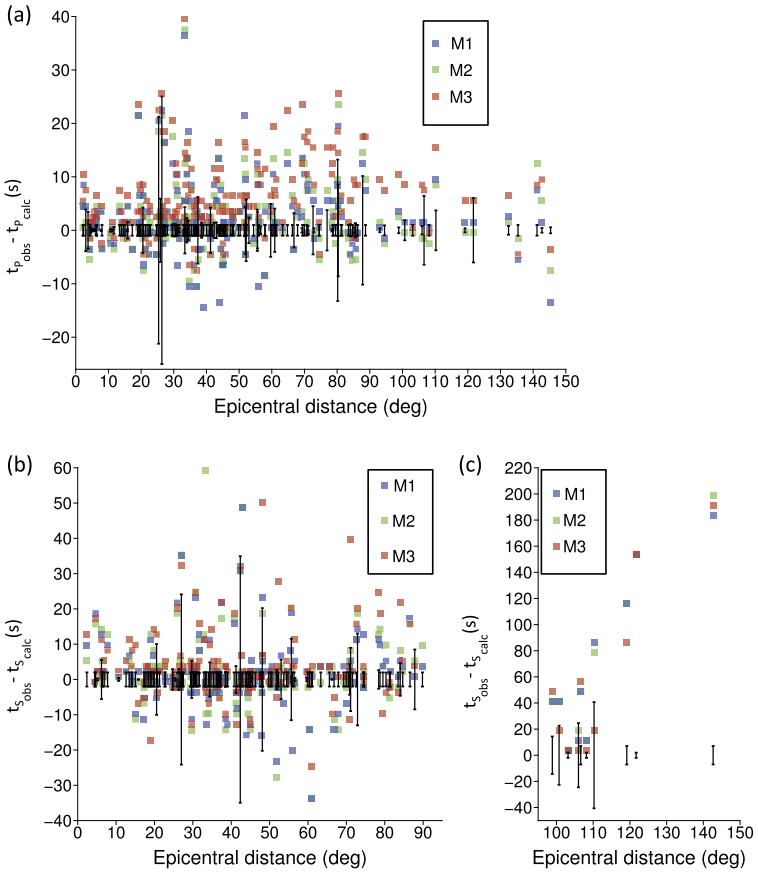

Fig. 11 Differences between observed and computed travel times as a function of epicentral distance for (**a**) *P* waves and (**b**)–(**c**) *S* waves. Vertical black lines indicate uncertainties on observed *P* wave and *S* wave travel times. M1, M2, and M3 results are shown in blue, green and red, respectively. The computed travel times shown here are for the maximum a posteriori model for each of the model suites M1, M2, and M3

3. In the mid-to-lower mantle (depth range 600–1200 km), the seismic profiles for all three models generally overlap over the entire range, indicative of a relatively uniform lower mantle with no clear evidence for a mid-mantle discontinuity as suggested in earlier studies (Nakamura 1983; Khan and Mosegaard 2002). Both the model based only on seismological data (M1) and the one relying on mineral physics assumption (M3) agree on that point.
4. Below ∼1200 km depth model variability increases for all three models and indicates the maximum depth to which the seismic wave speeds are properly constrained by the seismic travel time data set.
5. A relatively strong decrease in seismic wave speed at the base of the mantle is apparent in M1 and M3. In the case of M1 and M2, this velocity decrease is driven by having to fit strongly positive residual P- and S-wave travel times at large epicentral distances, whereas for M3 a "soft" zone is required to explain the Love number. While geophysical evidence for partial melt in the deep lunar interior is accumulating (Nakamura et al. 1973; Williams et al. 2001a; Efroimsky 2012b,a; Khan et al. 2014; Harada et al. 2014), models using

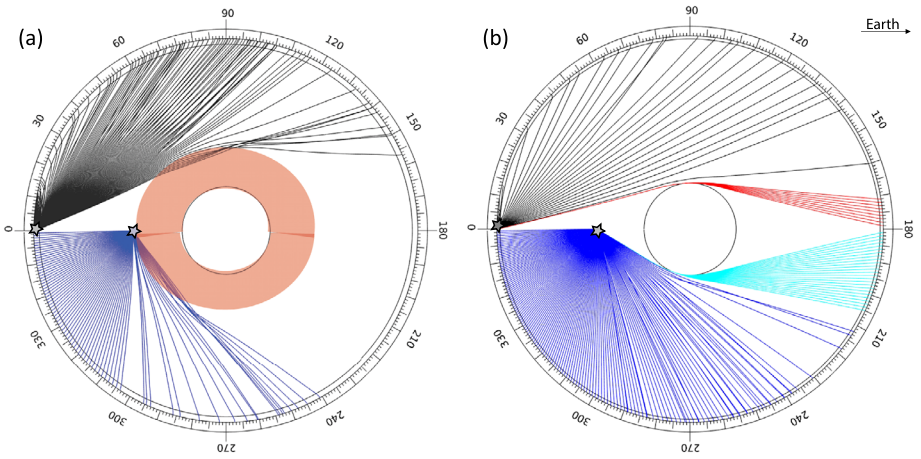

Fig. 12 Theoretical S-wave ray paths in models with and without a lower mantle low-velocity layer for a surface impact (gray star) and a deep moonquake (blue star), respectively. (**a**) model M1 with a low-velocity lower mantle (red region surrounding the core) and (**b**) model M2 without. For model M1, S-wave ray paths (black lines) are shown for a surface source and a source at 900 km (blue lines). For model M2, ray paths for S-waves are shown in black (surface source) and blue (source at 900 km depth) and for diffracted S-waves in red (surface source) and cyan (source at 900 km depth). The circle in the center marks the core in both plots. Plots were produced using the numerical software TTBox (Knapmeyer 2004)

different rheologies are also able to reproduce the geophysical observations (Nimmo et al. 2012).

7. While the models are capable of fitting the P wave arrivals at large epicentral distances, none of them are able to fit the strongly delayed S-wave travel times (Fig. 11), even in the case of models M1 and M3, that contain very low S-wave velocities at the base of the mantle. Because these travel times emanate from a single farside meteoroid impact and a farside deep moonquake, it suggests that the S-wave arrival time readings for these particular events are wrongly picked in the coda because the otherwise abrupt S-wave arrival has been attenuated. A possible explanation for this, includes either a lower mantle with a partial melt layer, which would strongly attenuate S-waves and create a shadow zone so as to render these difficult to observe or, alternatively, a large core that diffracts P-waves and produces arrivals at large distances, while the amplitude of diffracted S-waves decreases quickly with distance and provide an explanation for the absence of clear S-wave arrivals at large distances. These effects are illustrated in Fig. 12, which shows ray paths for S-waves in a model with (M1) and without (M2) a lower mantle low-velocity layer. A shadow zone is clearly present in the case of M1, whereas the effects of diffracted waves are seen in the case of M2.
8. Only model suites M2 and M3 are capable of constraining density structure. As in the case of seismic wave speeds, M3 is denser than M2 over most of the upper and mid-mantle. While the M2 distribution in the core region is wider than M3, densities overlap and suggest average core densities in the range 4–5 g/cm^3. Densities in this range are incompatible with a pure Fe core, but suggest a small core (∼350 km in radius) consisting of Fe with a substantial amount of light elements (Fig. 3b). From the data considered here, it is not possible to resolve an inner core since neither density nor absolute P-wave speed are well constrained in this region.

L_1-based misfit values for the three inversions are shown in Fig. 10. As expected, models M3 misfit values are significantly higher than both M2 and M1 given that models M3 are not obtained by inversion of the seismic travel time data. Despite different parameterizations and different crustal structure, models M1 and M2 produce similar misfit values with the more flexible parameterization of M1 resulting in the lowest misfit values. Based on this, we can make the following observations: (1) a seismic discontinuity separating crust and upper mantle is not necessarily required by the travel time data, although it should be noted that there are other arguments based on the seismic data that favour a discontinuity, e.g., crust-mantle body wave conversions and amplitude considerations, (Vinnik et al. 2001; Khan and Mosegaard 2002); (2) that uncertainties on the Apollo seismic travel time readings allow for a relatively large model spread; and (3) core size and composition (density) continue to remain elusive due to the general scarcity of data that directly sense the core and, not least, a lunar moment of inertia that is almost equal to that of a homogeneous sphere. Nevertheless, current consensus (Table 1) suggests a core 350 ± 40 km in radius with an Fe-like composition.

To better model lateral heterogeneities beneath stations, P- and S-wave station corrections have been applied to all travel times. The average P- and S-wave correction is set zero to avoid biasing velocity model estimates. Figure 13 summarises the inverted station corrections. These are broadly distributed for M1 and more peaked for the M2 models that invoke stronger prior constraints (note that M3 does not use station corrections). The consistency between the corrections of the different models is not ensured for all stations nor is its sign, i.e., whether positive or negative. These observations suggest that the station corrections are likely absorbing a number of effects including lateral heterogeneities between stations, variations of these heterogeneities with incidence angle, event mislocations and any other instrument or site effect at a given station. The variations of these parameters between M1 and M2 inversions and for the different velocity models of a given inversion suggest that these estimates are correlated to the inverted velocity model.

The low velocity layer at the top of the mantle is interpreted in terms of over-adiabatic thermal gradient. To do so, the excess thermal gradient relative to the adiabatic gradient as a function of lithosphere thickness are shown for the 1% best models of M2 in Fig. 14. The distribution clearly shows two types of models: models with thick lithospheres and low values of over-adiabatic thermal gradients, and models with thin lithospheres and large over-adiabatic thermal gradients. The low velocity layer is driven by this second set of models, among which the best models parameters correspond to an over-adiabatic thermal gradient value of 0.7 ± 0.4 °C/km, translating into a thermal gradient of about 1.7 ± 0.4 °C/km, in a lithosphere extending down to 260 km depth (1425 km radius). This value is slightly larger than the $\approx$1.3 °C/km temperature gradient estimates by Khan et al. (2006a) and Kuskov and Kronrod (1998), the only studies presenting a similar upper mantle low velocity layer. Moreover, these values are close to the value of about 1.4 °C/km obtained by Laneuville et al. (2013) for the region below Procellarum KREEP Terrane (PKT) where the Apollo seismic network is mainly located. This overall agreement suggests that the low velocity layer observed by Apollo seismic network may be linked to the presence of the PKT region.

7 Conclusion and Outlook

In this study, we have provided an overview of lunar seismicity, internal structure models, including scattering and attenuation properties of crust and mantle, lunar geophysical data

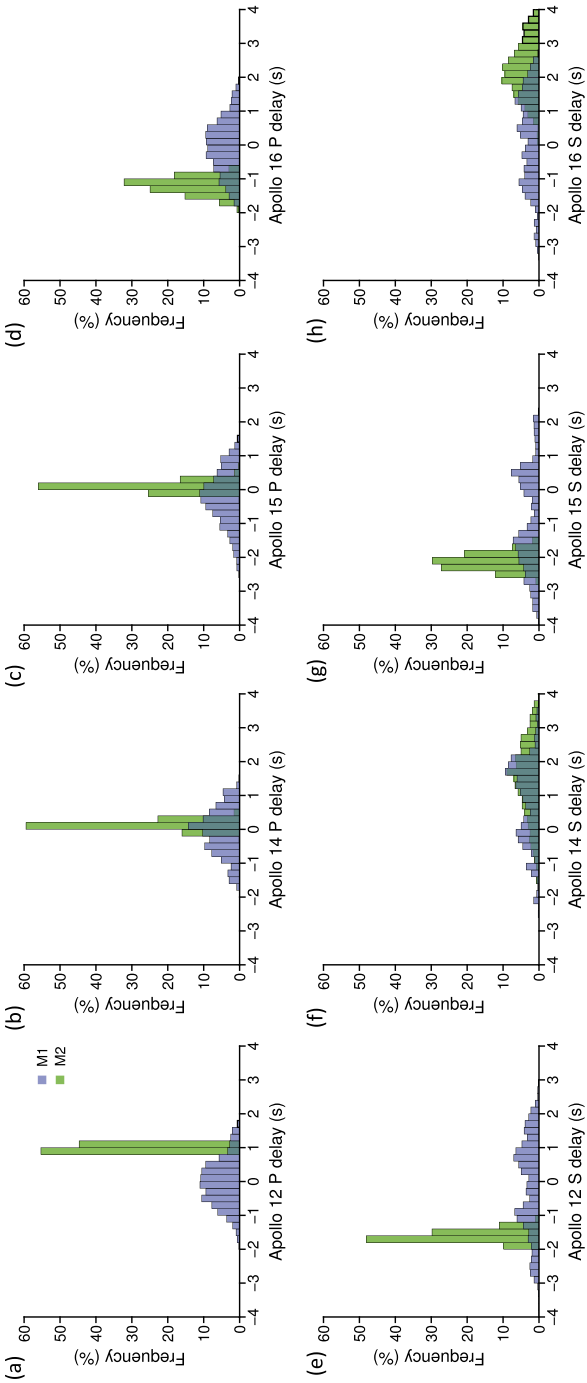

Fig. 13 Distributions of *P*-wave (**a**–**d**) and *S*-wave (**e**–**h**) station corrections for model suites M1 and M2. No station corrections were used for M3

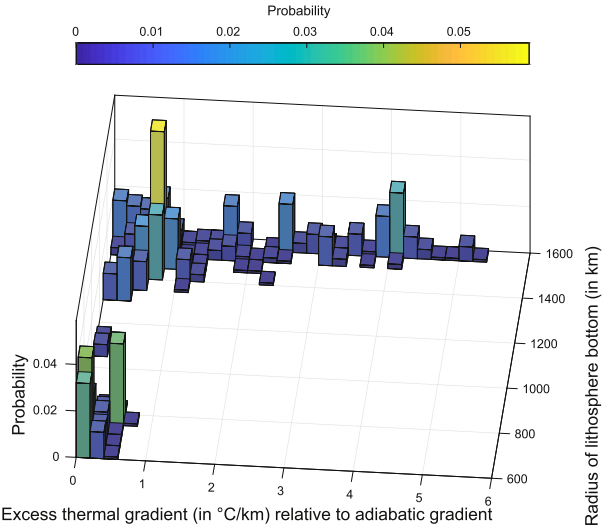

Fig. 14 2D histogram of excess thermal gradient (in °C/km) as a function of bottom radius of the lithosphere (in km) for the 1% best models of M2 inversion

sets other than the seismic data, and information pertinent to the lunar interior from modeling studies and laboratory measurements.

The comparison between the various seismic wave speed and attenuation models shows similarities and discrepancies. For example, crustal thickness in the vicinity of Apollo stations 12 and 14 appears to be constrained to within 10 km with a currently favoured thickness of between 30–40 km. Since a significant part of the seismic data illuminate upper and mid-mantle, models tend to overlap most in this particular region. Deep mantle and core structure are poorly constrained mainly due to the lack of seismic data at large epicentral distances. However, the models of seismic attenuation and scattering appear to present a relatively consistent picture in which the intrinsic attenuation inside the Moon is very low ($Q > 1500$) at all depths, and scattering is dominated by fracturing in the crust and upper mantle down to ∼100 km depth. In summary, large uncertainties persist and future studies relying on expanded and improved data will have to refine present results.

As part of this re-assessment, we also performed an inversion of the "new" body wave travel time data presented in our companion paper (Nunn et al. submitted) as a first step toward a unified reference model of the lunar interior. Three very different model parameterisations were used of which two of the investigated models considered geodetic and electromagnetic sounding data. Comparison between model outputs suggests that, despite large error bars on the arrival time data set, the first 600 km of the lunar interior appears to be relatively consistent between the models with evidence for a low-velocity zone in the 100–250 km depth range. The observed velocity decrease corresponds to a thermal gradient (∼1.7 °C/km), consistent with previous investigations (Khan et al. 2006a; Kuskov and Kronrod 1998), and could possibly be linked to the thermal structure (high abundance of heat-producing elements) below the lunar nearside region known as the Procellarum KREEP Terrane (Laneuville et al. 2013).

As a caveat, we should note that our model inversions were performed under the assumption of perfectly known event locations. This is a rather strong assumption, which was invoked for the purpose of comparing different interior structure parameterisations. Clearly, this assumption needs to be relaxed in future applications given the inherent trade-off between event locations and interior structure. Deep moonquake locations, in particular, are strongly model dependent.

Finally, analysis of the lunar seismic data will continue to improve our knowledge of the lunar interior, although significant improvement in our understanding will probably have to await the return of a new set of high-quality seismic data. Preferably, these data should be acquired from a spatially and temporally extended network of large-bandwidth stations to address some of the outstanding issues, such as crustal structure and layering, mantle discontinuities, lateral variations and mantle heterogeneities, and core size and composition. To ensure that high-quality instruments can be operated simultaneously, a set of low-level requirements have been produced by our team that are described in our companion paper (Nunn et al. submitted).

Acknowledgements We acknowledge ISSI Bern and ISSI Beijing for providing support to our international research team. This work was granted access to the HPC resources of CINES under the allocation A0050407341 made by GENCI. Internal structure models and quake locations presented in this study are available in electronic form at the following https://doi.org/10.5281/zenodo.3372489.

Appendices

A.1 Appendix

This appendix provides the numerical values of the median of internal structure model distributions of M1, M2, and M3 inversions.

Table 11 Seismic velocity (in km/s) and density (in g/cm^{-3}) models as a function of depth (in km) extracted from M1, M2 and M3 inversions. M1 and M2 models show the median values of the distributions, as well as the 1σ uncertainties. For M3 the best misfit model is shown

M1			M2				M3			
Depth (km)	V_P (km/s)	V_S (km/s)	Depth (km/s)	V_P (km/s)	V_S (km/s)	ρ (g/cm^{-3})	Depth (km)	V_P (km/s)	V_S (km/s)	ρ (g/cm^{-3})
0.00	4.04	2.32	0.00	1.00	0.50	2.60	0.00	4.50	2.47	2.60
10.00	4.65	2.68	1.00	1.00	0.50	2.60	20.00	5.70	3.12	2.76
20.00	5.26	3.05	1.00	3.20	1.80	2.60	40.00	6.73	3.71	2.89
30.00	5.90	3.42	12.00	3.20	1.80	2.60	60.00	7.62	4.30	3.23
40.00	6.51	3.79	12.00	5.50	3.30	2.60	80.00	7.62	4.30	3.23
50.00	7.10	4.12	28.00	5.50	3.30	2.60	100.00	7.63	4.31	3.23
60.00	7.57	4.38	28.00	7.68	4.41	3.34	120.00	7.80	4.45	3.35
70.00	7.62	4.42	41.63	7.68	4.41	3.34	140.00	7.80	4.45	3.35
80.00	7.63	4.42	65.40	7.68	4.40	3.34	160.00	7.80	4.45	3.36
90.00	7.64	4.42	90.00	7.67	4.39	3.34	180.00	7.80	4.44	3.36
100.00	7.64	4.42	110.00	7.66	4.39	3.34	200.00	7.81	4.44	3.36
110.00	7.64	4.41	132.01	7.66	4.39	3.34	220.00	7.81	4.44	3.36
120.00	7.64	4.41	140.59	7.67	4.39	3.34	240.00	7.88	4.48	3.36
130.00	7.64	4.41	176.44	7.68	4.39	3.34	260.00	7.98	4.52	3.41
140.00	7.64	4.40	180.99	7.69	4.40	3.35	280.00	8.03	4.53	3.42

Table 11 (*Continued*)

M1			M2				M3			
Depth (km)	V_P (km/s)	V_S (km/s)	Depth (km/s)	V_P (km/s)	V_S (km/s)	ρ (g/cm^{-3})	Depth (km)	V_P (km/s)	V_S (km/s)	ρ (g/cm^{-3})
150.00	7.63	4.40	201.10	7.70	4.41	3.35	300.00	8.03	4.53	3.42
160.00	7.63	4.39	224.75	7.71	4.41	3.35	320.00	8.04	4.53	3.42
170.00	7.63	4.39	243.07	7.72	4.42	3.35	340.00	8.04	4.53	3.42
180.00	7.63	4.38	275.40	7.74	4.43	3.36	360.00	8.04	4.53	3.42
190.00	7.62	4.38	290.00	7.75	4.43	3.36	380.00	8.05	4.53	3.42
200.00	7.62	4.38	310.00	7.76	4.44	3.36	400.00	8.05	4.53	3.42
210.00	7.62	4.38	330.00	7.78	4.45	3.36	420.00	8.05	4.53	3.43
220.00	7.62	4.38	350.00	7.79	4.45	3.37	440.00	8.05	4.53	3.43
230.00	7.62	4.37	370.00	7.80	4.46	3.37	460.00	8.05	4.53	3.43
240.00	7.62	4.37	390.00	7.82	4.47	3.37	480.00	8.05	4.53	3.43
250.00	7.62	4.37	410.00	7.83	4.47	3.37	500.00	8.06	4.53	3.43
260.00	7.62	4.37	429.66	7.84	4.48	3.38	520.00	8.06	4.53	3.43
270.00	7.62	4.37	446.83	7.85	4.49	3.38	540.00	8.06	4.53	3.43
280.00	7.63	4.37	488.22	7.86	4.50	3.38	560.00	8.06	4.53	3.43
290.00	7.64	4.37	495.88	7.87	4.50	3.38	580.00	8.06	4.53	3.43
300.00	7.64	4.37	501.10	7.88	4.51	3.39	600.00	8.06	4.53	3.43
310.00	7.65	4.37	514.69	7.89	4.51	3.39	620.00	8.06	4.53	3.43
320.00	7.65	4.37	542.72	7.91	4.52	3.39	640.00	8.06	4.53	3.44
330.00	7.66	4.38	563.71	7.92	4.53	3.39	660.00	8.06	4.53	3.44
340.00	7.67	4.38	585.59	7.93	4.53	3.39	680.00	8.06	4.52	3.44
350.00	7.68	4.38	619.69	7.94	4.54	3.40	700.00	8.06	4.52	3.44
360.00	7.69	4.39	639.98	7.95	4.54	3.40	720.00	8.06	4.52	3.44
370.00	7.70	4.39	650.00	7.96	4.55	3.40	740.00	8.06	4.52	3.44
380.00	7.71	4.39	670.00	7.97	4.55	3.40	760.00	8.05	4.51	3.44
390.00	7.72	4.40	690.00	7.98	4.55	3.40	780.00	8.06	4.51	3.44
400.00	7.73	4.40	710.00	7.99	4.56	3.41	800.00	8.05	4.51	3.44
410.00	7.74	4.41	735.10	8.00	4.57	3.41	820.00	8.05	4.51	3.44
420.00	7.75	4.41	750.00	8.01	4.57	3.41	840.00	8.05	4.51	3.44
430.00	7.76	4.42	775.40	8.02	4.57	3.41	860.00	8.05	4.51	3.44
440.00	7.77	4.42	790.00	8.02	4.58	3.41	880.00	8.04	4.50	3.44
450.00	7.78	4.43	810.00	8.03	4.58	3.41	900.00	8.04	4.50	3.44
460.00	7.79	4.43	830.00	8.04	4.59	3.42	920.00	8.04	4.49	3.44
470.00	7.80	4.44	850.00	8.05	4.59	3.42	940.00	8.04	4.49	3.44
480.00	7.81	4.44	870.00	8.06	4.59	3.42	960.00	8.03	4.49	3.44
490.00	7.82	4.45	890.00	8.06	4.60	3.42	980.00	8.03	4.48	3.44
500.00	7.84	4.45	910.00	8.07	4.60	3.42	1000.00	8.03	4.48	3.44
510.00	7.85	4.46	930.00	8.08	4.61	3.42	1020.00	8.02	4.48	3.44
520.00	7.86	4.46	950.00	8.09	4.61	3.43	1040.00	8.02	4.48	3.44
530.00	7.87	4.47	970.00	8.09	4.61	3.43	1060.00	8.02	4.48	3.44
540.00	7.88	4.47	990.00	8.10	4.61	3.43	1080.00	8.02	4.48	3.44
550.00	7.89	4.48	1010.00	8.11	4.62	3.43	1100.00	8.02	4.47	3.44

Table 11 (*Continued*)

M1			M2				M3			
Depth (km)	V_P (km/s)	V_S (km/s)	Depth (km/s)	V_P (km/s)	V_S (km/s)	ρ (g/cm^{-3})	Depth (km)	V_P (km/s)	V_S (km/s)	ρ (g/cm^{-3})
560.00	7.90	4.48	1030.00	8.11	4.62	3.43	1120.00	8.01	4.47	3.44
570.00	7.91	4.49	1050.00	8.12	4.63	3.43	1140.00	8.01	4.47	3.44
580.00	7.92	4.49	1070.00	8.12	4.63	3.43	1160.00	7.98	4.46	3.44
590.00	7.93	4.50	1090.00	8.13	4.64	3.44	1180.00	7.89	4.45	3.39
600.00	7.94	4.51	1110.00	8.14	4.65	3.44	1200.00	7.80	4.43	3.37
610.00	7.96	4.51	1130.00	8.14	4.66	3.44	1220.00	7.74	4.39	3.35
620.00	7.97	4.52	1150.00	8.15	4.66	3.44	1240.00	7.72	4.36	3.34
630.00	7.98	4.52	1170.00	8.15	4.67	3.44	1260.00	6.28	2.81	3.32
640.00	7.99	4.53	1190.00	8.16	4.68	3.44	1280.00	5.80	2.45	3.29
650.00	8.00	4.54	1210.00	8.16	4.69	3.44	1300.00	5.48	2.20	3.26
660.00	8.01	4.54	1230.00	8.17	4.69	3.44	1447.52	5.48	2.20	3.26
670.00	8.02	4.55	1237.10	8.17	4.70	3.44	1447.52	2.64	0.00	4.48
680.00	8.03	4.55	1237.10	8.18	4.70	3.44	1737.00	2.64	0.00	4.48
690.00	8.04	4.56	1257.10	8.18	4.68	3.45				
700.00	8.05	4.57	1277.10	8.17	4.58	3.45				
710.00	8.06	4.57	1297.10	8.14	4.52	3.45				
720.00	8.08	4.58	1317.10	4.00	0.00	4.16				
730.00	8.09	4.59	1337.10	4.00	0.00	4.38				
740.00	8.10	4.59	1357.10	4.00	0.00	4.46				
750.00	8.11	4.60	1377.10	4.00	0.00	4.54				
760.00	8.13	4.61	1397.10	4.00	0.00	4.54				
770.00	8.14	4.62	1417.10	4.00	0.00	4.55				
780.00	8.15	4.62	1437.10	4.00	0.00	4.55				
790.00	8.16	4.63	1457.10	4.00	0.00	4.55				
800.00	8.17	4.64	1477.10	4.00	0.00	4.55				
810.00	8.21	4.67	1497.10	4.00	0.00	4.55				
820.00	8.22	4.67	1517.10	4.00	0.00	4.55				
830.00	8.24	4.68	1537.10	4.00	0.00	4.55				
840.00	8.24	4.69	1557.10	4.00	0.00	4.55				
850.00	8.24	4.69	1577.10	4.00	0.00	4.55				
860.00	8.24	4.69	1597.10	4.00	0.00	4.55				
870.00	8.24	4.69	1617.10	4.00	0.00	4.55				
880.00	8.24	4.69	1637.10	4.00	0.00	4.55				
890.00	8.23	4.69	1657.10	4.00	0.00	4.55				
900.00	8.23	4.68	1677.10	4.00	0.00	4.55				
910.00	8.21	4.66	1697.10	4.00	0.00	4.55				
920.00	8.17	4.63	1717.10	4.00	0.00	4.55				
930.00	8.11	4.60	1737.10	4.00	0.00	4.55				
940.00	8.05	4.57								
950.00	7.99	4.54								
960.00	7.92	4.51								

Table 11 (*Continued*)

M1			M2				M3			
Depth (km)	V_P (km/s)	V_S (km/s)	Depth (km/s)	V_P (km/s)	V_S (km/s)	ρ (g/cm^{-3})	Depth (km)	V_P (km/s)	V_S (km/s)	ρ (g/cm^{-3})
970.00	7.84	4.47								
980.00	7.76	4.44								
990.00	7.69	4.40								
1000.00	7.66	4.37								
1010.00	7.63	4.36								
1020.00	7.60	4.36								
1030.00	7.60	4.38								
1040.00	7.60	4.39								
1050.00	7.64	4.40								
1060.00	7.65	4.40								
1070.00	7.62	4.38								
1080.00	7.59	4.37								
1090.00	7.57	4.37								
1100.00	7.53	4.36								
1110.00	7.52	4.35								
1120.00	7.49	4.37								
1130.00	7.49	4.39								
1140.00	7.50	4.43								
1150.00	7.51	4.45								
1160.00	7.55	4.47								
1170.00	7.56	4.49								
1180.00	7.52	4.46								
1190.00	7.54	4.45								
1200.00	7.55	4.45								
1210.00	7.36	4.36								
1220.00	7.29	4.31								
1230.00	7.24	4.24								
1240.00	7.20	4.19								
1250.00	7.12	4.12								
1260.00	7.05	4.00								
1270.00	6.99	3.93								
1280.00	6.94	3.84								
1290.00	6.88	3.73								
1300.00	6.80	3.57								
1310.00	6.71	0.00								
1410.00	5.32	0.00								
1510.00	5.32	0.00								
1610.00	5.32	0.00								
1710.00	5.32	0.00								
1737.00	5.32	0.00								

References

K. Aki, B. Chouet, Origin of coda waves: source, attenuation, and scattering effects. J. Geophys. Res. **80**(23), 3322–3342 (1975)

D. Antonangeli, G. Morard, N.C. Schmerr, T. Komabayashi, M. Krisch, G. Fiquet, Y. Fei, Toward a mineral physics reference model for the Moon's core, in *Proceedings of the National Academy of Sciences* (2015)

J. Besserer, F. Nimmo, M.A. Wieczorek, R.C. Weber, W.S. Kiefer, P.J. McGovern, J.C. Andrews-Hanna, D.E. Smith, M.T. Zuber, GRAIL gravity constraints on the vertical and lateral density structure of the lunar crust. Geophys. Res. Lett. **41**, 5771–5777 (2014). https://doi.org/10.1002/2014GL060240

J.-F. Blanchette-Guertin, C.L. Johnson, J.F. Lawrence, Investigation of scattering in lunar seismic coda. J. Geophys. Res., Planets **117**, 06003 (2012). https://doi.org/10.1029/2011JE004042

J.-F. Blanchette-Guertin, C. Johnson, J. Lawrence, Modeling seismic energy propagation in highly scattering environments. J. Geophys. Res., Planets **120**(3), 515–537 (2015)

A.S. Buono, D. Walker, The Fe-rich liquidus in the Fe–FeS system from 1 bar to 10 GPa. Geochim. Cosmochim. Acta **75**(8), 2072–2087 (2011)

H. Chi, R. Dasgupta, M.S. Duncan, N. Shimizu, Partitioning of carbon between Fe-rich alloy melt and silicate melt in a magma ocean—implications for the abundance and origin of volatiles in Earth, Mars, and the Moon. Geochim. Cosmochim. Acta **139**(Supplement C), 447–471 (2014)

J.A.D. Connolly, The geodynamic equation of state: what and how. Geochem. Geophys. Geosyst. **10**(10) (2009). Q10014. https://doi.org/10.1029/2009GC002540

M.R. Cooper, R.L. Kovach, J.S. Watkins, Lunar near-surface structure. Rev. Geophys. Space Phys. **12**, 291–308 (1974). https://doi.org/10.1029/RG012i003p00291

A.M. Dainty, M.N. Toksöz, K.R. Anderson, P.J. Pines, Y. Nakamura, G. Latham, Seismic scattering and shallow structure of the Moon in oceanus procellarum. Moon **9**, 11–29 (1974). https://doi.org/10.1007/BF00565388

A.M. Dainty, N.R. Goins, M.N. Toksöz, *Seismic Investigation of the Lunar Interior*, vol. 7 (1976a), p. 181

A.M. Dainty, M.N. Toköz, S. Stein, *Seismic Investigation of the Lunar Interior*, vol. 3 (1976b), pp. 3057–3075

M. Drilleau, E. Beucler, A. Mocquet, O. Verhoeven, G. Moebs, G. Burgos, J.-P. Montagner, P. Vacher, A bayesian approach to infer radial models of temperature and anisotropy in the transition zone from surface wave dispersion curves. Geophys. J. Int. **195**(2), 1165–1183 (2013). https://doi.org/10.1093/gji/ggt284

A. Duba, H.C. Heard, R.N. Schock, Electrical conductivity of orthopyroxene to 1400 C and the resulting selenotherm, in *Lunar and Planetary Science Conference Proceedings*, ed. by D.C. Kinsler Lunar and Planetary Science Conference Proceedings, vol. 7 (1976), pp. 3173–3181

F. Duennebier, G.H. Sutton, Thermal moonquakes. J. Geophys. Res. **79**, 4351–4363 (1974). https://doi.org/10.1029/JB079i029p04351

P. Dyal, C.W. Parkin, W.D. Daily, Structure of the lunar interior from magnetic field measurements, in *Lunar and Planetary Science Conference Proceedings*, ed. by D.C. Kinsler Lunar and Planetary Science Conference Proceedings, vol. 7 (1976), pp. 3077–3095

M. Efroimsky, Bodily tides near spin-orbit resonances. Celest. Mech. Dyn. Astron. **112**, 283–330 (2012a). https://doi.org/10.1007/s10569-011-9397-4

M. Efroimsky, Tidal dissipation compared to seismic dissipation: in small bodies, earths, and super-earths. Astrophys. J. **746**, 150 (2012b). https://doi.org/10.1088/0004-637X/746/2/150

Y. Fei, E. Brosh, Experimental study and thermodynamic calculations of phase relations in the Fe–C system at high pressure. Earth Planet. Sci. Lett. **408**(0), 155–162 (2014)

C. Frohlich, Y. Nakamura, Possible extra-Solar-System cause for certain lunar seismic events. Icarus **185**, 21–28 (2006). https://doi.org/10.1016/j.icarus.2006.07.002

J. Gagnepain-Beyneix, P. Lognonné, H. Chenet, D. Lombardi, T. Spohn, A seismic model of the lunar mantle and constraints on temperature and mineralogy. Phys. Earth Planet. Inter. **159**, 140–166 (2006). https://doi.org/10.1016/j.pepi.2006.05.009

R. Garcia, H. Tkalčić, S. Chevrot, A new global PKP data set to study Earth's core and deep mantle. Phys. Earth Planet. Inter. **159**, 15–31 (2006)

R.F. Garcia, J. Gagnepain-Beyneix, S. Chevrot, P. Lognonné, Very preliminary reference Moon model. Phys. Earth Planet. Inter. **188**, 96–113 (2011). https://doi.org/10.1016/j.pepi.2011.06.015

M.S. Ghiorso, M.M. Hirschmann, P.W. Reiners, V.C. Kress III, The pMELTS: a revision of melts for improved calculation of phase relations and major element partitioning related to partial melting of the mantle to 3 GPa. Geochem. Geophys. Geosyst. **3**(5), 1–35 (2002). https://doi.org/10.1029/2001GC000217

K. Gillet, L. Margerin, M. Calvet, M. Monnereau, Scattering attenuation profile of the Moon: implications for shallow moonquakes and the structure of the megaregolith. Phys. Earth Planet. Inter. **262**, 28–40 (2017). https://doi.org/10.1016/j.pepi.2016.11.001

N.R. Goins, Lunar seismology: the internal structure of the Moon. Ph.D. thesis, Mass. Inst. of Technol., Cambridge (1978)

N.R. Goins, A.M. Dainty, M.N. Toksoz, Lunar seismology—the internal structure of the Moon. J. Geophys. Res. **86**, 5061–5074 (1981). https://doi.org/10.1029/JB086iB06p05061

D.H. Green, N.G. Ware, W.O. Hibberson, A. Major, Experimental petrology of Apollo 12 basalts: part 1, sample 12009. Earth Planet. Sci. Lett. **13**(1), 85–96 (1971)

Y. Harada, S. Goossens, K. Matsumoto, J. Yan, J. Ping, H. Noda, J. Haruyama, Strong tidal heating in an ultralow-viscosity zone at the core-mantle boundary of the Moon. Nat. Geosci. **7**, 569–572 (2014). https://doi.org/10.1038/ngeo2211

E.H. Hauri, A.E. Saal, M.J. Rutherford, J.A. Van Orman, Water in the Moon's interior: truth and consequences. Earth Planet. Sci. Lett. **409**, 252–264 (2015). https://doi.org/10.1016/j.epsl.2014.10.053

S. Hempel, M. Knapmeyer, A.R.T. Jonkers, J. Oberst, Uncertainty of Apollo deep moonquake locations and implications for future network designs. Icarus **220**, 971–980 (2012)

B.A. Hobbs, L.L. Hood, F. Herbert, C.P. Sonett, An upper bound on the radius of a highly electrically conducting lunar core. J. Geophys. Res. **88**, 97–102 (1983). https://doi.org/10.1029/JB088iS01p00B97

L.L. Hood, Geophysical constraints on the lunar interior, in *Origin of the Moon*, ed. by W.K. Hartmann, R.J. Phillips, G.J. Taylor, 1986, pp. 361–410

L.L. Hood, F. Herbert, C.P. Sonett, The deep lunar electrical conductivity profile—structural and thermal inferences. J. Geophys. Res. **87**, 5311–5326 (1982). https://doi.org/10.1029/JB087iB07p05311

L.L. Hood, D.L. Mitchell, R.P. Lin, M.H. Acuna, A.B. Binder, Initial measurements of the lunar induced magnetic dipole moment using Lunar Prospector magnetometer data. Geophys. Res. Lett. **26**, 2327–2330 (1999). https://doi.org/10.1029/1999GL900487

L.L. Hood, M.T. Zuber, in *Recent Refinements in Geophysical Constraints on Lunar Origin and Evolution*, ed. by R.M. Canup, K. Righter, et al. (2000), pp. 397–409

P. Horvath, Analysis of lunar seismic signals—determination of instrumental parameters and seismic velocity distributio. Ph.D. thesis, Univ. of Tex. at Dallas, Richardson (1979)

J.S. Huebner, A. Duba, L.B. Wiggins, Electrical conductivity of pyroxene which contains trivalent cations—laboratory measurements and the lunar temperature profile. J. Geophys. Res. **84**, 4652–4656 (1979). https://doi.org/10.1029/JB084iB09p04652

Z. Jing, Y. Wang, Y. Kono, T. Yu, T. Sakamaki, C. Park, M.L. Rivers, S.R. Sutton, G. Shen, Sound velocity of Fe–S liquids at high pressure: implications for the Moon's molten outer core. Earth Planet. Sci. Lett. **396**, 78–87 (2014)

H. Kanamori, A. Nur, D. Chung, D. Wones, G. Simmons, Elastic wave velocities of lunar samples at high pressures and their geophysical implications. Science **167**, 726–728 (1970)

S.-i. Karato, Water distribution across the mantle transition zone and its implications for global material circulation. Earth Planet. Sci. Lett. **301**, 413–423 (2011). https://doi.org/10.1016/j.epsl.2010.11.038

S.-i. Karato, Geophysical constraints on the water content of the lunar mantle and its implications for the origin of the Moon. Earth Planet. Sci. Lett. **384** (2013). https://doi.org/10.1016/j.epsl.2013.10.001

T. Kawamura, N. Kobayashi, S. Tanaka, P. Lognonné, Lunar Surface Gravimeter as a lunar seismometer: investigation of a new source of seismic information on the Moon. J. Geophys. Res., Planets **120**, 343–358 (2015). https://doi.org/10.1002/2014JE004724

A. Khan, K. Mosegaard, An inquiry into the lunar interior: a nonlinear inversion of the Apollo lunar seismic data. J. Geophys. Res., Planets **107**, 3-1–3-23 (2002). https://doi.org/10.1029/2001JE001658

A. Khan, K. Mosegaard, Further constraints on the deep lunar interior. Geophys. Res. Lett. **32**, 22203 (2005). https://doi.org/10.1029/2005GL023985

A. Khan, T.J. Shankland, A geophysical perspective on mantle water content and melting: inverting electromagnetic sounding data using laboratory-based electrical conductivity profiles. Earth Planet. Sci. Lett. **317**, 27–43 (2012). https://doi.org/10.1016/j.epsl.2011.11.031

A. Khan, K. Mosegaard, K.L. Rasmussen, A new seismic velocity model for the Moon from a Monte Carlo inversion of the Apollo lunar seismic data. Geophys. Res. Lett. **27**, 1591–1594 (2000). https://doi.org/10.1029/1999GL008452

A. Khan, K. Mosegaard, J.G. Williams, P. Lognonné, Does the Moon possess a molten core? Probing the deep lunar interior using results from LLR and Lunar Prospector. J. Geophys. Res., Planets **109**, 09007 (2004). https://doi.org/10.1029/2004JE002294

A. Khan, J.A.D. Connolly, N. Olsen, K. Mosegaard, Constraining the composition and thermal state of the Moon from an inversion of electromagnetic lunar day-side transfer functions. Earth Planet. Sci. Lett. **248**(3), 579–598 (2006b). https://doi.org/10.1016/j.epsl.2006.04.008

A. Khan, J. Maclennan, S.R. Taylor, J.A.D. Connolly, Are the Earth and the moon compositionally alike? Inferences on lunar composition and implications for lunar origin and evolution from geophysical modeling. J. Geophys. Res., Planets **111**(E5), E05005 (2006a). https://doi.org/10.1029/2005JE002608

A. Khan, J.A.D. Connolly, J. Maclennan, K. Mosegaard, Joint inversion of seismic and gravity data for lunar composition and thermal state. Geophys. J. Int. **168**, 243–258 (2007). https://doi.org/10.1111/j.1365-246X.2006.03200.x

A. Khan, A. Pommier, G.A. Neumann, K. Mosegaard, The lunar moho and the internal structure of the Moon: a geophysical perspective. Tectonophysics **609**, 331–352 (2013). https://doi.org/10.1016/j.tecto.2013.02.024. Moho: 100 years after Andrija Mohorovicic

A. Khan, J.A.D. Connolly, A. Pommier, J. Noir, Geophysical evidence for melt in the deep lunar interior and implications for lunar evolution. J. Geophys. Res., Planets **119**(10), 2197–2221 (2014). https://doi.org/10.1002/2014JE004661

M. Knapmeyer, TTBox: a Matlab toolbox for the computation of 1D teleseismic travel times. Seismol. Res. Lett. **75**(6), 726–733 (2004). https://doi.org/10.1785/gssrl.75.6.726

T. Komabayashi, Thermodynamics of melting relations in the system Fe–FeO at high pressure: implications for oxygen in the Earth's core. J. Geophys. Res., Solid Earth **2014**, 010980 (2014)

A.S. Konopliv, R.S. Park, D.-N. Yuan, S.W. Asmar, M.M. Watkins, J.G. Williams, E. Fahnestock, G. Kruizinga, M. Paik, D. Strekalov, N. Harvey, D.E. Smith, M.T. Zuber, The JPL lunar gravity field to spherical harmonic degree 660 from the GRAIL primary mission. J. Geophys. Res., Planets **118**, 1415–1434 (2013). https://doi.org/10.1002/jgre.20097

R.L. Kovach, J.S. Watkins, Apollo 17 seismic profiling: probing the lunar crust. Science **180**, 1063–1064 (1973a). https://doi.org/10.1126/science.180.4090.1063

R.L. Kovach, J.S. Watkins, The structure of the lunar crust at the Apollo 17 site, in *Lunar and Planetary Science Conference Proceedings*, vol. 4 (1973b), p. 2549

V.A. Kronrod, O.L. Kuskov, Inversion of seismic and gravity data for the composition and core sizes of the Moon. Izv. Phys. Solid Earth **47**, 711–730 (2011). https://doi.org/10.1134/S1069351311070044

O.L. Kuskov, D.K. Belashchenko, Thermodynamic properties of Fe–S alloys from molecular dynamics modeling: implications for the lunar fluid core. Phys. Earth Planet. Inter. **258**, 43–50 (2016). https://doi.org/10.1016/j.pepi.2016.07.006

O.L. Kuskov, V.A. Kronrod, Constitution of the Moon5. Constraints on composition, density, temperature, and radius of a core. Phys. Earth Planet. Inter. **107**, 285–306 (1998). https://doi.org/10.1016/S0031-9201(98)00082-X

O.L. Kuskov, V.A. Kronrod, Geochemical constraints on the model of the composition and thermal conditions of the Moon according to seismic data. Izv. Phys. Solid Earth **45**, 753–768 (2009). https://doi.org/10.1134/S1069351309090043

D.R. Lammlein, Lunar seismicity and tectonics. Phys. Earth Planet. Inter. **14**, 224–273 (1977). https://doi.org/10.1016/0031-9201(77)90175-3

M. Laneuville, M.A. Wieczorek, D. Breuer, N. Tosi, Asymmetric thermal evolution of the Moon. J. Geophys. Res., Planets **118**, 1435–1452 (2013). https://doi.org/10.1002/jgre.20103

M. Laneuville, M.A. Wieczorek, D. Breuer, J. Aubert, G. Morard, T. Rückriemen, A long-lived lunar dynamo powered by core crystallization. Earth Planet. Sci. Lett. **401**, 251–260 (2014)

M. Laneuville, J. Taylor, M.A. Wieczorek, Distribution of radioactive heat sources and thermal history of the Moon. J. Geophys. Res., Planets **123**(12), 3144–3166 (2018). https://doi.org/10.1029/2018JE005742

E. Larose, A. Khan, Y. Nakamura, M. Campillo, Lunar subsurface investigated from correlation of seismic noise. Geophys. Res. Lett. **32**, 16201 (2005). https://doi.org/10.1029/2005GL023518

G.V. Latham, M. Ewing, F. Press, G. Sutton, J. Dorman, Y. Nakamura, N. Toksöz, R. Wiggins, J. Derr, F. Duennebier, Passive seismic experiment. Science **167**(3918), 455–457 (1970a). https://doi.org/10.1126/science.167.3918.455

G. Latham, M. Ewing, J. Dorman, F. Press, N. Toksöz, G. Sutton, R. Meissner, F. Duennebier, Y. Nakamura, R. Kovach, M. Yates, Seismic data from man-made impacts on the Moon. Science **170**(3958), 620–626 (1970b). https://doi.org/10.1126/science.170.3958.620

F.G. Lemoine, S. Goossens, T.J. Sabaka, J.B. Nicholas, E. Mazarico, D.D. Rowlands, B.D. Loomis, D.S. Chinn, D.S. Caprette, G.A. Neumann, D.E. Smith, M.T. Zuber, High-degree gravity models from GRAIL primary mission data. J. Geophys. Res., Planets **118**, 1676–1698 (2013). https://doi.org/10.1002/jgre.20118

F.G. Lemoine, S. Goossens, T.J. Sabaka, J.B. Nicholas, E. Mazarico, D.D. Rowlands, B.D. Loomis, D.S. Chinn, G.A. Neumann, D.E. Smith, M.T. Zuber, GRGM900C: a degree 900 lunar gravity model from GRAIL primary and extended mission data. Geophys. Res. Lett. **41**, 3382–3389 (2014). https://doi.org/10.1002/2014GL060027

P. Lognonné, C.L. Johnson, Planetary seismology. Treatise Geophys. **10**, 69–122 (2007)

P. Lognonné, J. Gagnepain-Beyneix, H. Chenet, A new seismic model of the Moon: implications for structure, thermal evolution and formation of the Moon. Earth Planet. Sci. Lett. **211**, 27–44 (2003). https://doi.org/10.1016/S0012-821X(03)00172-9

J. Longhi, Petrogenesis of picritic mare magmas: constraints on the extent of early lunar differentiation. Geochim. Cosmochim. Acta **70**(24), 5919–5934 (2006)

L. Margerin, G. Nolet, Multiple scattering of high-frequency seismic waves in the deep earth: Modeling and numerical examples. J. Geophys. Res., Solid Earth **108**(B5) (2003). https://doi.org/10.1029/2002JB001974

K. Matsumoto, R. Yamada, F. Kikuchi, S. Kamata, Y. Ishihara, T. Iwata, H. Hanada, S. Sasaki, Internal structure of the Moon inferred from Apollo seismic data and selenodetic data from GRAIL and LLR. Geophys. Res. Lett. **42**, 7351–7358 (2015). https://doi.org/10.1002/2015GL065335

I. Matsuyama, F. Nimmo, J.T. Keane, N.H. Chan, G.J. Taylor, M.A. Wieczorek, W.S. Kiefer, J.G. Williams, GRAIL, LLR, and LOLA constraints on the interior structure of the Moon. Geophys. Res. Lett. **43**, 8365–8375 (2016). https://doi.org/10.1002/2016GL069952

E. Mazarico, M.K. Barker, G.A. Neumann, M.T. Zuber, D.E. Smith, Detection of the lunar body tide by the Lunar Orbiter Laser Altimeter. Geophys. Res. Lett. **41**, 2282–2288 (2014). https://doi.org/10.1002/2013GL059085

K. Miljković, M.A. Wieczorek, G.S. Collins, S.C. Solomon, D.E. Smith, M.T. Zuber, Excavation of the lunar mantle by basin-forming impact events on the Moon. Earth Planet. Sci. Lett. **409**, 243–251 (2015). https://doi.org/10.1016/j.epsl.2014.10.041

G. Morard, J. Bouchet, A. Rivoldini, D. Antonangeli, M. Roberge, E. Boulard, A. Denoeud, M. Mezouar, Liquid properties in the Fe–FeS system under moderate pressure: tool box to model small planetary cores. Am. Mineral. **103**(11), 1770–1779 (2018). https://doi.org/10.2138/am-2018-6405

K. Mosegaard, A. Tarantola, Monte Carlo sampling of solutions to inverse problems. J. Geophys. Res., Solid Earth **100**(B7), 12431–12447 (1995). https://doi.org/10.1029/94JB03097

Y. Nakamura, Seismic energy transmission in the lunar surface zone determined from signals generated by movement of lunar rovers. Bull. Seismol. Soc. Am. **66**, 593–606 (1976)

Y. Nakamura, Seismic velocity structure of the lunar mantle. J. Geophys. Res. **88**, 677–686 (1983). https://doi.org/10.1029/JB088iB01p00677

Y. Nakamura, Farside deep moonquakes and deep interior of the Moon. J. Geophys. Res. **110** (2005). https://doi.org/10.1029/2004JE002332

Y. Nakamura, in *Planetary Seismology: Early Observational Results*, ed. by V.C.H. Tong, R.A.E. García (Cambridge University Press, Cambridge, 2015), pp. 91–106. https://doi.org/10.1017/CBO9781107300668.010

Y. Nakamura, J. Koyama, Seismic Q of the lunar upper mantle. J. Geophys. Res. **87**, 4855–4861 (1982). https://doi.org/10.1029/JB087iB06p04855

Y. Nakamura, D. Lammlein, G. Latham, M. Ewing, J. Dorman, F. Press, N. Toksoz, New seismic data on the state of the deep lunar interior. Science **181**, 49–51 (1973). https://doi.org/10.1126/science.181.4094.49

Y. Nakamura, G. Latham, D. Lammlein, M. Ewing, F. Duennebier, J. Dorman, Deep lunar interior inferred from recent seismic data. Geophys. Res. Lett. **1**, 137–140 (1974). https://doi.org/10.1029/GL001i003p00137

Y. Nakamura, F.K. Duennebier, G.V. Latham, H.J. Dorman, Structure of the lunar mantle. J. Geophys. Res. **81**, 4818–4824 (1976). https://doi.org/10.1029/JB081i026p04818

Y. Nakamura, G.V. Latham, H.J. Dorman, A.-B.K. Ibrahim, J. Koyama, P. Horvath, Shallow moonquakes—depth, distribution and implications as to the present state of the lunar interior, in *Lunar and Planetary Science Conference, 10th, Houston, Tex., March 19–23, 1979, Proceedings*, vol. 3 (1979), pp. 2299–2309

Y. Nakamura, G.V. Latham, H.J. Dorman, Apollo lunar seismic experiment—final summary, in *Lunar and Planetary Science Conference Proceedings*, ed. by W.V. Boynton, T.J. Ahrens. Lunar and Planetary Science Conference Proceedings, vol. 13 (1982), p. 117

F. Nimmo, U.H. Faul, E.J. Garnero, Dissipation at tidal and seismic frequencies in a melt-free Moon. J. Geophys. Res. **117**, 09005 (2012). https://doi.org/10.1029/2012JE004160

K. Nishida, A. Suzuki, H. Terasaki, Y. Shibazaki, Y. Higo, S. Kuwabara, Y. Shimoyama, M. Sakurai, M. Ushioda, E. Takahashi, T. Kikegawa, D. Wakabayashi, N. Funamori, Towards a consensus on the pressure and composition dependence of sound velocity in the liquid Fe–S system. Phys. Earth Planet. Inter. **257**, 230–239 (2016)

C. Nunn, R.F. Garcia, Y. Nakamura, A.G. Marusiak, T. Kawamura, D. Sun, L. Margerin, R. Weber, , M. Drilleau, M.A. Wieczorek, A. Khan, A. Rivoldini, P. Lognonne, P. Zhu, Lunar seismology: a data and instrumentation review. Space Sci. Rev. (submitted)

J. Oberst, Meteoroids near the Earth–Moon System as Inferred from Temporal and Spatial Distribution of Impacts Detected by the Lunar Seismic Network. Ph.D. thesis, Univ. of Tex. at Austin (1989)

J.-P. Poirier, *Introduction to the Physics of the Earth's Interior* (2000), p. 326
N. Rai, W. van Westrenen, Lunar core formation: new constraints from metal–silicate partitioning of siderophile elements. Earth Planet. Sci. Lett. **388**(0), 343–352 (2014)
A. Ricolleau, Y. Fei, A. Corgne, J. Siebert, J. Badro, Oxygen and silicon contents of Earth's core from high pressure metal-silicate partitioning experiments. Earth Planet. Sci. Lett. **310**(3–4), 409–421 (2011)
K. Righter, M.J. Drake, Core formation in Earth's Moon, Mars, and Vesta. Icarus **124**, 513–529 (1996)
K. Righter, B.M. Go, K.A. Pando, L. Danielson, D.K. Ross, Z. Rahman, L.P. Keller, Phase equilibria of a low s and C lunar core: implications for an early lunar dynamo and physical state of the current core. Earth Planet. Sci. Lett. **463**, 323–332 (2017)
M. Sambridge, Geophysical inversion with a neighbourhood algorithm—I. Searching a parameter space. Geophys. J. Int. **138**, 479–494 (1999). https://doi.org/10.1046/j.1365-246X.1999.00876.x
H. Sato, M.C. Fehler, T. Maeda, *Seismic Wave Propagation and Scattering in the Heterogeneous Earth* (Springer, Berlin, 2012)
A. Scheinberg, K.M. Soderlund, G. Schubert, Magnetic field generation in the lunar core: the role of inner core growth. Icarus **254**, 62–71 (2015)
P.C. Sellers, Seismic evidence for a low-velocity lunar core. J. Geophys. Res. **97**, 11663–11672 (1992)
C. Sens-Schönfelder, E. Larose, Temporal changes in the lunar soil from correlation of diffuse vibrations. Phys. Rev. E **78**(4), 045601 (2008). https://doi.org/10.1103/PhysRevE.78.045601
P.M. Shearer, *Introduction to Seismology*, 2nd edn. (Cambridge University Press, Cambridge, 2009). https://doi.org/10.1017/CBO9780511841552
H. Shimizu, M. Matsushima, F. Takahashi, H. Shibuya, H. Tsunakawa, Constraint on the lunar core size from electromagnetic sounding based on magnetic field observations by an orbiting satellite. Icarus **222**, 32–43 (2013). https://doi.org/10.1016/j.icarus.2012.10.029
Y. Shimoyama, H. Terasaki, S. Urakawa, Y. Takubo, S. Kuwabara, S. Kishimoto, T. Watanuki, A. Machida, Y. Katayama, T. Kondo, Thermoelastic properties of liquid Fe–C revealed by sound velocity and density measurements at high pressure. J. Geophys. Res., Solid Earth **121**(11), 7984–7995 (2016)
D.E. Smith, M.T. Zuber, G.B. Jackson, J.F. Cavanaugh, G.A. Neumann, H. Riris, X. Sun, R.S. Zellar, C. Coltharp, J. Connelly, R.B. Katz, I. Kleyner, P. Liiva, A. Matuszeski, E.M. Mazarico, J.F. McGarry, A.-M. Novo-Gradac, M.N. Ott, C. Peters, L.A. Ramos-Izquierdo, L. Ramsey, D.D. Rowlands, S. Schmidt, V.S. Scott, G.B. Shaw, J.C. Smith, J.-P. Swinski, M.H. Torrence, G. Unger, A.W. Yu, T.W. Zagwodzki, The Lunar Orbiter Laser Altimeter investigation on the Lunar Reconnaissance Orbiter mission. Space Sci. Rev. **150**, 209–241 (2010). https://doi.org/10.1007/s11214-009-9512-y
D. Sollberger, C. Schmelzbach, J.O.A. Robertsson, S.A. Greenhalgh, Y. Nakamura, A. Khan, The shallow elastic structure of the lunar crust: new insights from seismic wavefield gradient analysis. Geophys. Res. Lett. **43**(19), 10078–10087 (2016). https://doi.org/10.1002/2016GL070883
C.P. Sonett, Electromagnetic induction in the Moon. Rev. Geophys. Space Phys. **20**, 411–455 (1982). https://doi.org/10.1029/RG020i003p00411
F.D. Stacey, P.M. Davis, *Physics of the Earth* (2008)
E.S. Steenstra, Y. Lin, N. Rai, M. Jansen, W. van Westrenen, Carbon as the dominant light element in the lunar core. Am. Mineral. **102**(1), 92 (2017)
E.S. Steenstra, A.X. Seegers, J. Eising, B.G.J. Tomassen, F.P.F. Webers, J. Berndt, S. Klemme, S. Matveev, W. van Westrenen, Evidence for a sulfur-undersaturated lunar interior from the solubility of sulfur in lunar melts and sulfide-silicate partitioning of siderophile elements. Geochim. Cosmochim. Acta **231**, 130–156 (2018)
L. Stixrude, C. Lithgow-Bertelloni, Thermodynamics of mantle minerals—I. Physical properties. Geophys. J. Int. **162**, 610–632 (2005). https://doi.org/10.1111/j.1365-246X.2005.02642.x
S.R. Taylor, G.J. Taylor, L.A. Taylor, The Moon: a Taylor perspective. Geochim. Cosmochim. Acta **70**, 5904–5918 (2006). https://doi.org/10.1016/j.gca.2006.06.262
B. Tittmann, Lunar rock Q in 3000–5000 range achieved in laboratory. Philos. Trans. R. Soc., Math. Phys. Eng. Sci. **285**(1327), 475–479 (1977)
B. Tittmann, M. Abdel-Gawad, R. Housley, Elastic velocity and Q factor measurements on Apollo 12, 14, and 15 rocks, in *Lunar and Planetary Science Conference Proceedings*, vol. 3 (1972), pp. 2565–2575
B. Tittmann, J. Curnow, R. Housley, Internal friction quality factor Q greater than or equal to 3100 achieved in lunar rock 70215,85, in *Lunar and Planetary Science Conference Proceedings*, vol. 6 (1975), pp. 3217–3226
B. Tittmann, L. Ahlberg, J. Curnow, Internal friction and velocity measurements, in *Lunar and Planetary Science Conference Proceedings*, vol. 7 (1976), pp. 3123–3132
B. Tittmann, H. Nadler, J. Richardson, L. Ahlberg, Laboratory measurements of p-wave seismic Q on lunar and analog rocks, in *Lunar and Planetary Science Conference Proceedings*, vol. 9 (1978), pp. 3627–3635

M.N. Toksoz, A.M. Dainty, S.C. Solomon, K.R. Anderson, Structure of the Moon. Rev. Geophys. Space Phys. **12**, 539–567 (1974)

H. Urey, *The Planets: Their Origin and Development* (Yale University Press, New Haven, 1952), p. 245

M. van Kan Parker, C. Sanloup, N. Sator, B. Guillot, E.J. Tronche, J.-P. Perrillat, M. Mezouar, N. Rai, W. van Westrenen, Neutral buoyancy of titanium-rich melts in the deep lunar interior. Nat. Geosci. **5**, 186–189 (2012). https://doi.org/10.1038/ngeo1402

L. Vinnik, H. Chenet, J. Gagnepain-Beyneix, P. Lognonne, First seismic receiver functions on the Moon. Geophys. Res. Lett. **28**, 3031–3034 (2001). https://doi.org/10.1029/2001GL012859

H. Wang, T. Todd, D. Weidner, G. Simmons, Elastic properties of Apollo 12 rocks, in *Lunar and Planetary Science Conference Proceedings*, vol. 2 (1971), pp. 2327–2336

N. Warren, E. Schreiber, C. Scholz, J. Morrison, P. Norton, M. Kumazawa, O. Anderson, Elastic and thermal properties of Apollo 11 and Apollo 12 rocks, in *Lunar and Planetary Science Conference Proceedings*, vol. 2 (1971), p. 2345

R.C. Weber, P. Lin, E.J. Garnero, Q. Williams, P. Lognonné, Seismic detection of the lunar core. Science **331**, 309 (2011). https://doi.org/10.1126/science.1199375

M.A. Wieczorek, Gravity and topography of the terrestrial planets, in *Treatise on Geophysics*, 2nd edn., ed. by T. Spohn, G. Schubert, vol. 10 (Elsevier-Pergamon, Oxford, 2015), pp. 153–193. https://doi.org/10.1016/B978-0-444-53802-4.00169-X

M.A. Wieczorek, B.L. Jolliff, A. Khan, M.E. Pritchard, B.O. Weiss, J.G. Williams, L.L. Hood, K. Righter, C.R. Neal, C.K. Shearer, I.S. McCallum, S. Tompkins, B.R. Hawke, C. Peterson, J.J. Gillis, B. Bussey, The constitution and structure of the lunar interior. Rev. Mineral. Geochem. **60**, 221–364 (2006). https://doi.org/10.2138/rmg.2006.60.3

M.A. Wieczorek, G.A. Neumann, F. Nimmo, W.S. Kiefer, G.J. Taylor, H.J. Melosh, R.J. Phillips, S.C. Solomon, J.C. Andrews-Hanna, S.W. Asmar, A.S. Konopliv, F.G. Lemoine, D.E. Smith, M.M. Watkins, J.G. Williams, M.T. Zuber, The crust of the Moon as seen by GRAIL. Science **339**(6120), 671–675 (2013). https://doi.org/10.1126/science.1231530

J.G. Williams, D.H. Boggs, Tides on the Moon: theory and determination of dissipation. J. Geophys. Res., Planets **120**, 689–724 (2015). https://doi.org/10.1002/2014JE004755

J.G. Williams, D.H. Boggs, C.F. Yoder, J.T. Ratcliff, J.O. Dickey, Lunar rotational dissipation in solid body and molten core. J. Geophys. Res. **106**, 27933–27968 (2001a). https://doi.org/10.1029/2000JE001396

J.G. Williams, D.H. Boggs, C.F. Yoder, J.T. Ratcliff, J.O. Dickey, Lunar rotational dissipation in solid body and molten core. J. Geophys. Res. **106**, 27933–27968 (2001b)

J.G. Williams, D.H. Boggs, W.M. Folkner, De430 lunar orbit, physical librations, and surface coordinates. IOM 335-JW,DB,WF-20130722-016, Jet Propul. Lab., Pasadena, Calif., 22 July 2013

J.G. Williams, A.S. Konopliv, D.H. Boggs, R.S. Park, D.-N. Yuan, F.G. Lemoine, S. Goossens, E. Mazarico, F. Nimmo, R.C. Weber, S.W. Asmar, H.J. Melosh, G.A. Neumann, R.J. Phillips, D.E. Smith, S.C. Solomon, M.M. Watkins, M.A. Wieczorek, J.C. Andrews-Hanna, J.W. Head, W.S. Kiefer, I. Matsuyama, P.J. McGovern, G.J. Taylor, M.T. Zuber, Lunar interior properties from the GRAIL mission. J. Geophys. Res., Planets **119**, 1546–1578 (2014). https://doi.org/10.1002/2013JE004559

B.A. Wyatt, The melting and crystallisation behaviour of a natural clinopyroxene-ilmenite intergrowth. Contrib. Mineral. Petrol. **61**(1), 1–9 (1977)

T. Yoshino, Laboratory electrical conductivity measurement of mantle minerals. Surv. Geophys. **31**(2), 163–206 (2010). https://doi.org/10.1007/s10712-009-9084-0

T. Yoshino, T. Katsura, Re-evaluation of electrical conductivity of anhydrous and hydrous wadsleyite. Earth Planet. Sci. Lett. **337**, 56–67 (2012). https://doi.org/10.1016/j.epsl.2012.05.023

N. Zhao, P. Zhu, B. Zhang, Y. Yuan, Moonquake relocation. Earth Sci., J. China Univ. Geosci. **40**, 1276–1286 (2015)

S. Zhong, C. Qin, G. A, J. Wahr, Can tidal tomography be used to unravel the long-wavelength structure of the lunar interior? Geophys. Res. Lett. **39**(15) (2012). https://doi.org/10.1029/2012GL052362